

Bio-Nanomaterials: Understanding Key Biophysics and Their Applications

ANUPAM GIRI, NIRMAL GOSWAMI, SOUMIK SARKAR AND SAMIR KUMAR PAL*

ABSTRACT

At the interface between nanomaterials and biological systems, an understanding of the interactions between them is of significant interest. Nanoparticles interacting with small organic ligands, therapeutic molecules, proteins, DNA and cell membranes establish a series of nanoparticle/biological interfaces that depend on colloidal forces as well as dynamic biophysicochemical interactions. These interactions could impart unique physical properties to the nanomaterials and at the same time can also regulate biological responses of the bio-nanoconjugates. Studies aimed at correlating the properties of nanomaterials such as size, shape, physicochemical functionality, surface charge, and composition with bio-molecular structure/functionality provides a foundation for rational designing of the next-generation nano tools beneficial for advanced biological/technological applications. In this article, we will present our ultrafast spectroscopic investigations for the understanding of key biophysical processes in the interactions of nanomaterials with different biological systems to provide a perspective on the applications/long-term implications of the bio-nanomaterials in the diverse field of nanotechnology.

Key words: Protein-capped metal nanoparticles and nanoclusters, Ligand functionalized manganese oxide nanoparticles, Semiconductor based bio-nanoconjugates, Emergence of

Department of Chemical, Biological and Macromolecular Sciences, S.N. Bose National Centre for Basic Sciences, Block JD, Sector III, Salt Lake, Kolkata 700 098, India

*Corresponding author: E-mail: skpal@bose.res.in

novel optical/magnetic properties, Toxic metal ion sensing and Photocatalysis.

1. INTRODUCTION

The interface of biology and inorganic materials represents one of the fastest growing and most promising areas of nanotechnology. Since, nanomaterials can display distinct biological effects compared with bulk materials of the same chemical composition, the physico-chemical characterization of nanomaterials and the understanding of their interaction with biological media are essential for optimizing nanoparticles properties. The ‘nano-bio’ interface comprises dynamic physicochemical interactions, kinetics and thermodynamic exchanges between nanomaterial surfaces and the surfaces of biological components (for example small biomolecules, proteins, DNA etc.). Moreover, nanotechnology-based approaches are being explored for a variety of biomedical applications such as for drug delivery, bioimaging, tissue engineering and biosensors. A substantial number of these approaches employ nanoscale materials or bio-nanomaterials for developing unique functionalities required by the biomedical systems. For this field to evolve, we must understand the dynamic forces and molecular components that shape these interactions. In this chapter, we present our consistent efforts to explore how the interactions between nanomaterials and biological systems modify the fundamental forces that govern nanoparticle properties as well as their interactions. Furthermore, by employing ultrafast (picosecond/femtosecond time scales) spectroscopic technique, we define the excited state dynamical pathways of the migration of electronic radiation at the bio-nano interface. We introduce various bio-nanomaterials, discuss their potential applications, and finally present their future prospects.

2. METHODOLOGY

2.1. Characterization Techniques

Optical spectra of the solutions were taken with a Shimadzu Model UV-2450 spectrophotometer using a quartz cuvette of 1 cm path length. The characteristic fluorescence excitation and fluorescence emission spectra were recorded on a Jobin Yvon Model Fluoromax-3 fluorimeter.

TEM samples were prepared by dropping sample stock solutions onto a 300-mesh carbon coated copper grid and dried overnight in air. Particle sizes were determined from micrographs recorded using a FEI

TecnaiTF-20 field-emission high-resolution transmission electron microscope operating at 200 kV.

A JASCO FTIR-6300 spectrometer was used for the Fourier transform infrared spectroscopy (FTIR) to confirm the covalent attachment. For FTIR measurements, powdered samples were mixed with KBr powder and pelletized. The background correction was made by using a reference of KBr pellet.

Raman scattering measurements were performed in a back scattering geometry using a micro-Raman setup consists of a spectrometer (model LabRAM HR, JobinYvon) and a Peltier-cooled charge-coupled device (CCD) detector. An air cooled argon ion laser with a wavelength of 488 nm was used as the excitation light source. Raman spectra of all samples have been recorded at room temperature in the frequency range 50–4000 cm^{-1} .

DLS measurements were done with Nano S Malvern instrument employing a 4 mW He-Ne laser ($\lambda = 632.8 \text{ nm}$) equipped with a thermo stated sample chamber. All the scattered photons are collected at 173° scattering angle. The scattering intensity data are processed using the instrumental software to obtain the hydrodynamic diameter (d_H) and the size distribution of the scatterer in each sample. The instrument measures the time-dependent fluctuation in the intensity of light scattered from the particles in solution at a fixed scattering angle. Hydrodynamic diameter (d_H) of the proteins is estimated from the intensity autocorrelation function of the time-dependent fluctuation in intensity. d_H is defined as:

$$d_H = \frac{k_b T}{3\pi\eta D}$$

Where k_b is the Boltzmann constant, η is the viscosity, and D is the translational diffusion coefficient. In a typical size distribution graph from the DLS measurement, the X-axis shows a distribution of size classes in nm, while the Y-axis shows the relative intensity of the scattered light.

The CD spectrum were measured in a Jasco 815 spectropolarimeter with a Peltier setup for the temperature-dependent measurements.

Matrix-assisted laser desorption ionization mass spectrometry (MALDI-MS) studies were conducted using a Voyager-DE PRO

Biospectrometry Workstation from Applied Biosystems. A pulsed nitrogen laser of 337 nm was used for the MALDI-MS studies. Mass spectra were collected in positive-ion mode and were averaged for 100 shots.

Magnetic measurements were performed in a Lake Shore VSM with an electromagnet that can produce field up to 1.6T.

XRD patterns was obtained by employing a scanning rate of $0.02^\circ \text{ s}^{-1}$ in the 2θ range from 10° to 80° by PANalytical XPERT-PRO diffractometer equipped with Cu $K\alpha$ radiation (at 40 mA and 40 kV).

Fluorescence micrographs of the samples were taken using an Olympus BX51 fluorescence microscope employing 365 and 436 excitation wavelengths generated through WBS and WGS mirror units, respectively. During the capturing of fluorescence micrographs, in case of 365 and 436 nm wavelength excitation, integration times were kept constant.

XPS measurements were carried out using Omicron Nanotechnology instrument equipped with seven channeltrons with binding energy resolution of 0.1 eV. XPS were done using monochromatic Al $K\alpha$ X-rays (1486.6 eV). The X-rays source was at 15 keV with the emission current of the filament of 20 mA. All measurements were done at ultrahigh vacuum conditions of 5×10^{-10} mbar. Electron flooding was employed for sample charging compensation during the measurements. The binding energies were calibrated with respect to adventitious C 1s feature at 284.6 eV and internal oxygen peak. XPS spectra were deconvoluted to their individual components using Gaussian Lorentzian function after background subtraction with Shirley function in Casa XPS software.

Picosecond-resolved fluorescence transients were measured by using commercially available spectrophotometer (Life Spec-ps) from Edinburgh Instruments, UK for 375 nm excitation. For 293 nm excitation we have used the third harmonic laser beam of 879 nm (0.5 nJ per pulse) using a mode locked Ti-sapphire laser with an 80 MHz repetition rate (Tsunami, Spectra Physics), pumped by a 10 W Millennia (Spectra Physics) followed by a pulse-peaker (rate 8 MHz) and a third harmonic generator (Spectra Physics, model 3980). The third harmonic beam was used for excitation of the sample inside the Time-Correlated-Single-Photon-Counting (TCSPC) instrument (IRF=50 ps) and the second harmonic beam was collected for the start pulse. The observed fluorescence transients were fitted by using a nonlinear least square fitting procedure to a function ($X(t) = \int_0^t E(t')R(t-t')dt'$) comprising of

convolution of the IRF ($E(t)$) with a sum of exponential ($R(t) = A + \sum_{i=1}^N B_i e^{-t/\tau_i}$) with pre-exponential factors (B_i), characteristic lifetimes (τ_i) and a background (A). Relative concentration in a multi exponential decay was finally expressed as: $c_n = \frac{B_n}{\sum_{i=1}^N B_i} \times 100$. The quality of the curve fitting was evaluated by reduced chi-square and residual data. It has to be noted that with our time resolved instrument, we can resolve at least one fourth of the instrument response time constants after the de-convolution of the IRF.

2.2. Förster Resonance Energy Transfer (FRET) Technique

To estimate the FRET efficiency of the donor and hence to determine the distance of the donor-acceptor pair, we followed the methodology described in chapter 13 of Ref.^[1]. The Förster distance (R_0) is given by,

$$R_0 = 0.211 \left[\kappa^2 n^{-4} Q_D J(\lambda) \right]^{\frac{1}{6}} \text{..(in \AA)}, \quad (1)$$

where κ^2 is a factor describing the relative orientation in space of the transition dipoles of the donor and acceptor. We assumed that the orientation factor κ^2 is equal to the dynamic average of 2/3 which is not a major deviation from real fact of randomized donor and acceptor orientations in an ensemble. Moreover, a variation of κ^2 does not seem to have resulted in major errors in the calculated distances. The refractive index (n) of the medium was assumed to be 1.4. $J(\lambda)$, the overlap integral, which expresses the degree of spectral overlap between the donor emission and the acceptor absorption, is given by,

$$J(\lambda) = \frac{\int_0^{\infty} F_D(\lambda) \varepsilon(\lambda) \lambda^4 d\lambda}{\int_0^{\infty} F_D(\lambda) d\lambda} \quad (2)$$

where $F_D(\lambda)$ is the fluorescence intensity of the donor in the wavelength range of λ to $\lambda + d\lambda$ and is dimensionless. $\varepsilon(\lambda)$ is the extinction coefficient (in $M^{-1}cm^{-1}$) of the acceptor at λ . If λ is in nm, then J is in units of $M^{-1}cm^{-1}nm^4$.

Once the value of R_0 is known, the donor-acceptor distance (R) can easily be calculated using the formula,

$$R^6 = [R_0^6 (1 - E)] / E, \quad (3)$$

here E is FRET efficiency, measured by using the lifetimes of the donor in the absence (τ_D) and presence τ_{DA} of acceptor which is defined as,

$$E = 1 - (\tau_{DA} / \tau_D) \quad (4)$$

It has to be noted that eq. (4) holds rigorously only for a homogeneous system (*i.e.* identical donor–acceptor complexes) in which the donor and the donor–acceptor complex have single exponential decays. However, for donor–acceptor systems decaying with multi–exponential lifetimes, FRET efficiency (E) is calculated from the amplitude weighted lifetimes $\langle \tau \rangle = \sum_i \alpha_i \tau_i$, where α_i is the relative amplitude contribution to the lifetime τ_i . We have used the amplitude weighted time constants for τ_D and τ_{DA} to evaluate E using eq. (4).

3. TYPES OF BIO–NANOMATERIALS

3.1. Metallic Bio–Nanomaterials

3.1.1. *Au@Protein bio–nanoconjugates and exploration of key chemistry of the biomolecule*²

This study involves the facile preparation of “green” Au nanoparticles (NPs) in a number of protein solutions starting from globular proteins to enzyme and finally protein mixture extracted from Escherichia Coli, a gram negative bacterium, without the addition of any reducing agent. The nucleation of NPs in the protein environments, which is the consequence of electron transfer from protein to the metal ions, is observed to be dependent on the melting temperature of the host protein. However, time required to start the nucleation (induction time) is also found to be protein–specific. Here, we have attempted to rationalize the protein–assisted formation of NPs in a simple analytical model of autocatalysis. This model is evolving under the impudence of two distinct reactions. The first of these is the thermal denaturation of the protein structure under thermal condition and the second one is reversible autocatalytic process in which Au NP is the autocatalytic species (both the product and catalyst for the reaction). The obtained nanoparticles are characterized by ultraviolet–visible (UV–vis) absorption spectroscopy, high–resolution transmission electron microscopy (HRTEM). The change in the protein structure at various temperatures has been followed by circular dichroism (CD) spectroscopy. We have also demonstrated that the protein capped NPs can be utilized as an

efficient catalyst for the degradation of 4-nitrophenylacetate (4-NPA) using NaBH_4 as the hydrogen donor. The reduction of 4-NPA to 4-aminophenol is of industrial importance as 4-aminophenol is a commercially important intermediate for the manufacture of analgesic and antipyretic drugs. Although a number of researchers have extensively studied, the catalytic reduction of 4-nitrophenol (4-NP) by NaBH_4 using polymer/resin bead-supported metal NPs,³⁻⁶ the synthesis of protein capped Au NPs and the use of these NPs without any support for this catalytic purpose has not been attempted earlier. The kinetics of the catalysis is observed to follow Langmuir-Hinshelwood model of surface mediated catalysis reaction.

Synthesis of Au@protein bio-nanoconjugates

The Au@protein bio-nanoconjugates were prepared by the following procedure: 3 ml 20 μM protein solutions were prepared in 20 mM phosphate buffer solution. Then 60 μl 100 mM HAuCl_4 solution was added so that protein- HAuCl_4 ratio was maintained at 1:100. A detailed temperature dependent study was performed starting from 30°C for each mixture and it has been found that when the mixtures were heated at 76°C, 75°C and 60°C for HSA, BSA and SC respectively then the colors of the solutions were changed from light yellow to reddish brown. Such colour transition is indicative of changes in the metal oxidation state. In this case, Au (III) is reduced to Au (0) by protein in the phosphate buffer solution. We have not observed any sign of NP formation at room temperature for several days.

Figure 1a presents the TEM image of Au@HSA bio-nanoconjugates. The image reveals that the bio-nanoconjugates are almost spherical in shape and follow a uniform narrow size distribution. Particle sizes have been estimated by fitting our experimental TEM data to be 3.1 nm (inset in Fig 1a (right)). The corresponding HRTEM image of the particles is shown in Fig. 1b. The interplanar distance of the fringes is measured to be about 0.24 nm, consistent with the distance between the (111) planes of the gold crystal lattice. The image in the inset of Fig. 1b represents the corresponding selected area electron diffraction (SAED) pattern which confirms the crystallinity of those particles. It has to be noted that the average size of 3.1 nm Au NPs obtained in the Au@HSA NPs solution, is also confirmed from TEM and absorption studies. Thus in our experimental conditions, the possibility of formation of free larger Au NPs of micrometre size (due to uncontrolled growth) is negligibly small as they are not revealed in the TEM images of the sample. A typical energy-dispersive X-ray (EDAX) spectrum of Au@HSA sample is shown in the inset of Fig 1a (left) revealing the presence of Au. Fig. 1c

presents the HRTEM image of Au@BSA bio-nanoconjugates and the size distribution is shown as an inset of Fig. 1c.

It is well-known that the Au NPs of less than 10 nm exhibit a surface plasmon (SP) band in the visible region (~ 530 nm)⁷. A change in absorbance or wavelength of the SP band^[8–10] provides a measure of particle size, shape, concentration, and dielectric medium properties. Fig. 2a shows the UV-vis spectra of the Au NPs conjugated with HSA, BSA, SC and *E. coli* extract protein revealing surface plasmon bands at 530 nm, 531 nm, 540 nm and 600 nm respectively. Fig. 2b shows the UV-vis absorption spectra obtained at different time intervals after mixing with aqueous AuCl_4^- solution with HSA in phosphate buffer at 76°C temperature. Formation of Au nanoparticles in the colloidal solution was monitored from their absorption spectra as the small noble metal particles reveal absorption band in the UV-vis spectral

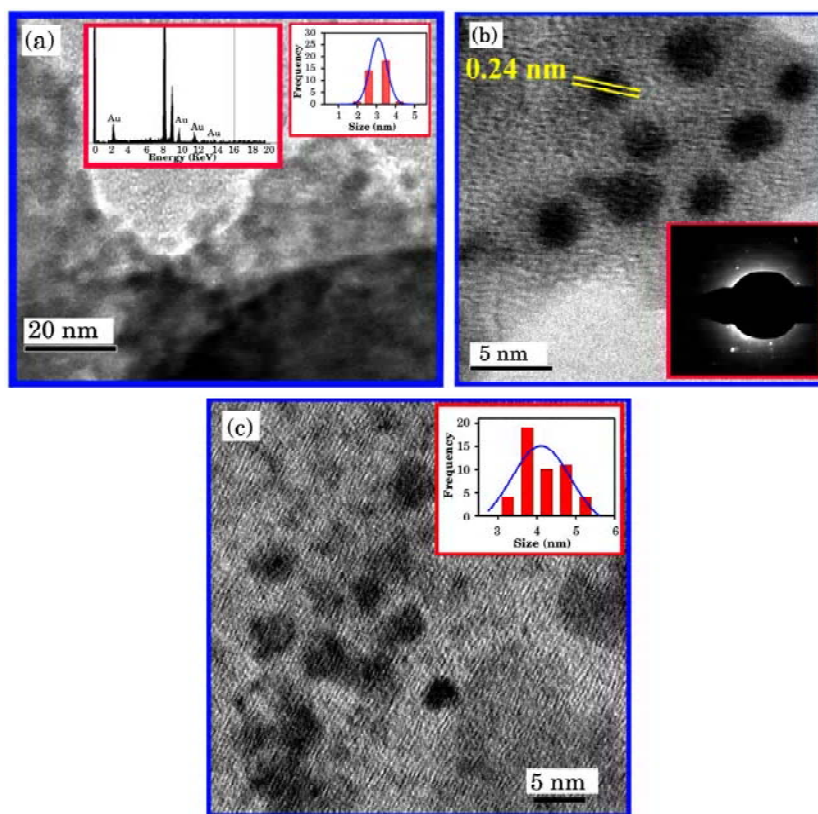


Fig. 1: (a) HRTEM of Au@HSA bio-nanoconjugates. The EDAX pattern (left) and the size distribution (right) of the sample are shown in the insets. (b) HRTEM image and SAED showing the crystalline structure of Au@HSA NPs. (c) HRTEM of Au@BSA bio-nanoconjugates. The size distribution of the sample is shown in the inset.

region due to surface plasmon resonance (SPR)¹¹. The sharp absorption band peaking at 530 nm indicates a relatively high monodispersity, both in size and shape of the Au particles¹², consistent with the HRTEM images.

Long time stability of the Au NP in aqueous solutions (for several months) indicates that the HSA serves as capping agent. In the case of the other proteins, a similar trend was observed as that of the HSA.

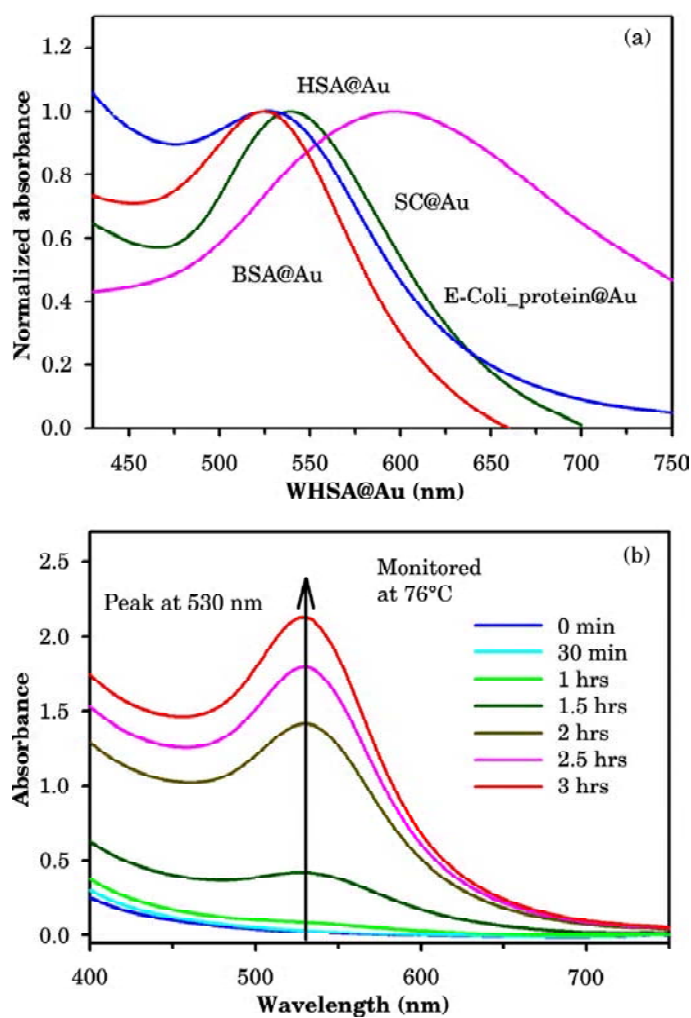
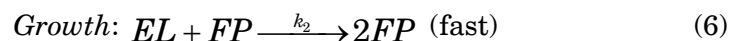
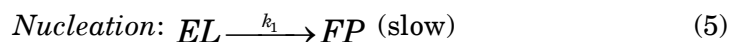


Fig. 2: (a) UV-vis spectra of Au NPs conjugated with various proteins, HSA, BSA, SC and *E. coli* extract respectively. (b) Time-resolved UV-vis spectra for one of the representative proteins (HSA) at 76°C.

Kinetics of nanoparticle formation

In the case of the autocatalytic reactions, the modified protein–salt conjugate serves as a substrate in reactions. The general mechanism of the nanoparticle formation can be written as shown in the following equations:



where, L represents the salt *i.e.*, AuCl_4^- , and E and F represent two different forms of protein where F–form is more perturbed than E–form, and k_1 and k_2 are the rate constants of the slow and fast step respectively. Here, EL denotes the protein–salt conjugate and FP denotes the protein nanoparticle conjugate. The corresponding rate equation (assuming first order reaction) of the first step can be written as,

$$[FP] = [EL]_0 (1 - \exp^{-k_1 t}) \quad (7)$$

where, $[EL]_0$ and $[FP]$ are the concentration of the E–form of the protein–salt conjugate at the initial time and the concentration of the protein nanoparticle conjugate at time = t respectively.

Equation 6 is the autocatalytic step¹³. For this autocatalytic reaction the concentration of the product can be written as,

$$[FP] = \frac{[EL]_0 + [FP]_0}{1 + \frac{[EL]_0}{[FP]_0} \exp^{-([EL]_0 + [FP]_0)k_2 t}} \quad (8)$$

So, the total concentration of the protein capped nanoparticles is obtained by the linear combination of equation (7) and equation (8) and thus it can be written as:

$$[FP] = m \times \left(\frac{[EL]_0 + [FP]_0}{1 + \frac{[EL]_0}{[FP]_0} \exp^{-([EL]_0 + [FP]_0)k_2 t}} \right) + n \times ([EL]_0 \times (1 - \exp^{-k_1 t})) \quad (9)$$

where, m and n denotes the contributions of the fast and slow step respectively.

The evolution of the optical density at 530 nm and 540 nm are presented for Au@HSA at 76°C and Au@SC at 60°C in Fig 3a and 3b

respectively. It is apparent that for Au@HSA the optical density increases very slowly upto 120 min for HSA, indicating an induction time (t_0), then sharply increases and finally saturates at a constant value which corresponds to a complete reduction stage. The induction time became shorter when the concentration of protein is increased. The most interesting information is the variation in induction period (shown in Fig. 3d) from protein to protein with same concentration. We assume that the size as well as the melting temperature is the predominant factor for the induction period. The denaturation of protein plays an important role in activating the reaction. From Fig. 3d, it is clear that proteins having low melting temperature have small induction time and vice versa. Second, based on the experimental results, we have proposed an analytical model for the kinetics of the Au@protein system which suggests that autocatalysis is involved for the synthesis process. This model suggests that during the induction period, nucleations of the NPs are slowly formed and can be considered as seeds. The formation of these nucleations, or seeds, catalyzes the reduction processes and thus in the next stage, seed-mediated nucleation and growth occur simultaneously, and the number of particles rapidly increases as the reaction progresses. Here, the strong capping property of the proteins inhibits the nanoparticle growth, thus generating high monodispersity. The solid lines in Fig. 3 refer to the fit of the experimental data with equation (9) while Table 1 shows the fitting parameters. This model gives a quantitative explanation of the kinetic data shown in Fig. 3 for all the proteins. In particular, it explains the dependence of induction time on the k_1 *i.e.*, higher the value of rate constant (k_1), smaller the induction time and vice versa. The autocatalytic rate constant (k_2) as revealed from Table 1, demonstrates that larger proteins (*i.e.*, HSA or BSA) are less active than smaller proteins (*i.e.*, SC, CHT or *E. coli* extract) for the growth of NPs. The overwhelming contribution of growth step compared to that of the nucleation is clear from Table 1. In simple autocatalytic reaction¹⁴ the overall rate is obtained by plotting $\ln[a/(1-a)]$ vs time,

Table 1: List of the parameters obtained from the analytical model of particle formation

Protein	k_1 (min^{-1})	k_2 ($M^{-1}\text{min}^{-1}$)	m (%)	n (%)
HSA	1.245×10^{-4}	0.015	0.91(91%)	0.09(9%)
SC	4.677×10^{-4}	0.020	0.79(79%)	0.21(21%)
<i>E. coli</i> extract	3.178×10^{-1}	3.488	0.72(72%)	0.28(28%)

where $a = (\text{O.D}(t)/\text{O.D}(\infty))$ and $\text{O.D}(t)$ and $\text{O.D}(\infty)$ are the optical densities at times t and ∞ , respectively. The rate constant (k_{obs}) is obtained from the slopes of these plots. In case of Au@HSA the value of k_{obs} is found to be 0.028 min^{-1} .

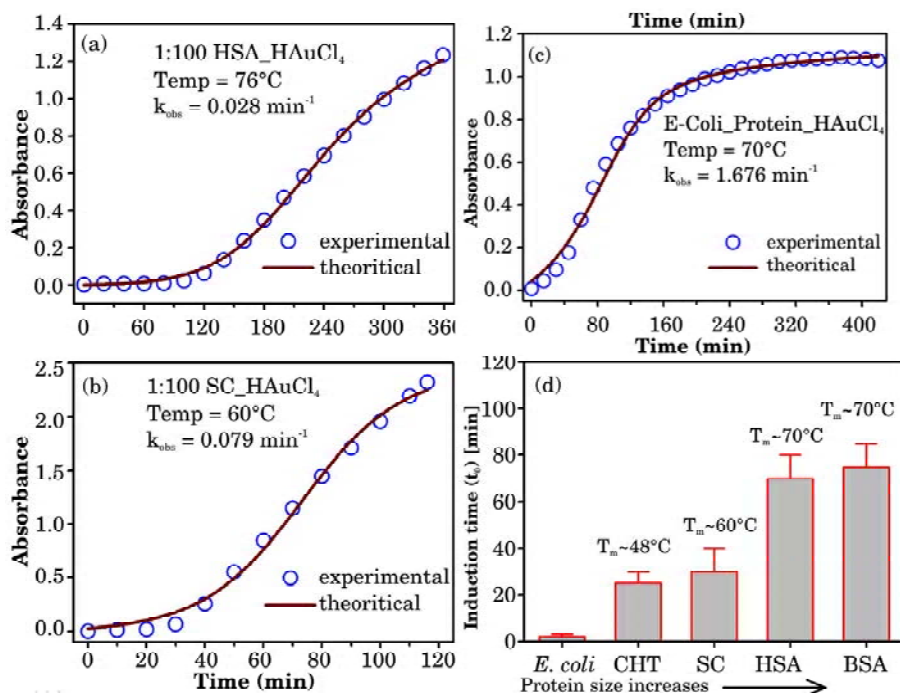
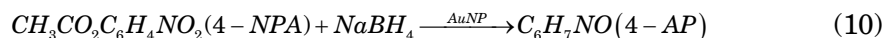


Fig. 3: (a) Time course of absorbance at 530 nm during the formation of Au NPs by HSA protein in phosphate buffer solution. (b) Similar curve at 540 nm by using SC in phosphate buffer solution. The red lines are the theoretical curves generated by using equation (9). Blue circles are the experimental data for HSA and SC NPs respectively. (c) Absorbance kinetics of the Au NPs formation at 580 nm using *E. coli* extract as reducing agent. (d) Plot of induction time for different proteins. In all the cases (except *E. coli*) the protein salt ratio has been maintained to 1:100 where the protein concentration is fixed at 20 mM.

Catalytic reduction of 4-nitrophenyl acetate (4-NPA) by Au bio-nanoconjugates

The catalytic reduction of 4-NPA by sodium borohydride onto the surface of the Au NPs is presented as,



In the present study, the obtained kinetic data of 4-NPA reduction are fitted in a first-order rate equation as an excess of borohydride is used compared to 4-NPA. The apparent rate constant (k_{app}) is assumed to be proportional to the surface area (S) of the metal nanoparticles present in the system^[15-17].

The catalytic function of Au@protein bio-nanoconjugates is substantiated by carrying out the reduction of aqueous 4-NPA, which has a peak at 276 nm in the UV-visible spectrum (Fig. 4a curve I). Addition of sodium borohydride to 4-NPA immediately results in a shift in the peak to 400 nm with intensification of yellow colour of the solution (Fig. 4a curve III) due to nitrophenolate ion formation. In the absence of any catalyst, the peak at 400 nm remained unaltered even for two days. Addition of Au@protein bio-nanoconjugates to the yellow colour of the nitrophenolate ion solution immediately results the diminution of 400 nm peak with intensification of a new peak at ~ 297 nm (Fig. 4a curve II) because of the reduction of 4-nitrophenolate species to 4-aminophenol (4-AP). A control experiment with denatured proteins devoid of gold nanoparticles did not provide any signature of 4-AP under the same experimental condition. The generation of 4-AP confirms the

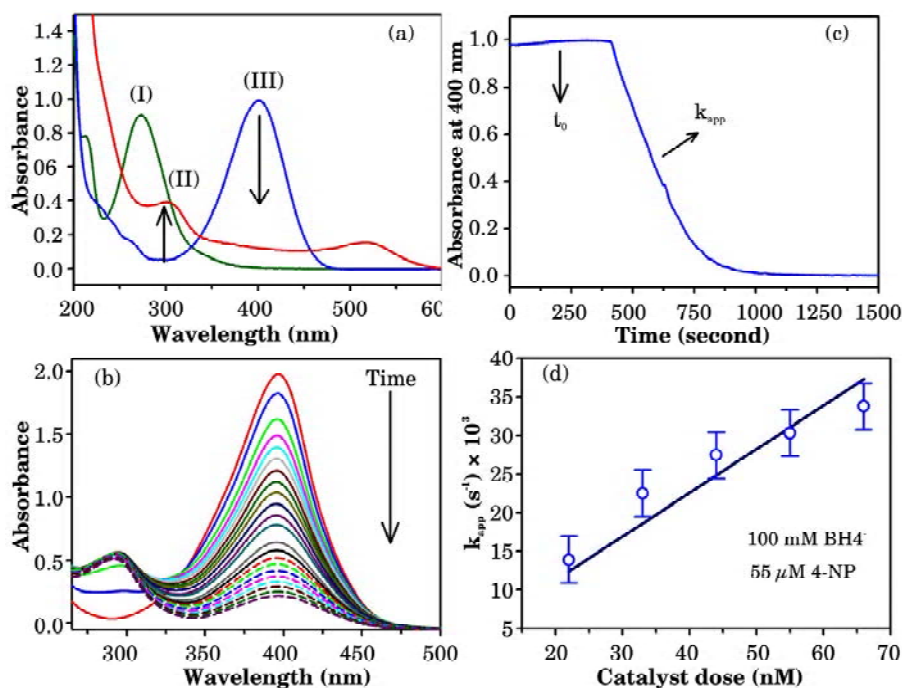


Fig. 4: (a) Absorption spectra of 4-NPA (I) in absence of NaBH₄, (III) in presence of NaBH₄ at 0 min and (II) in presence of Au@protein bio-nanoconjugates. Conditions: [4-NP] = 5.5×10^{-5} M; [Au NPs] = 2.2×10^{-7} M; [NaBH₄] = 0.1M. (b) Concentration versus time plot (monitored at 400 nm) for 4-NPA reduction by NaBH₄. Conditions: [4-NP] = 5.5×10^{-5} M; [NaBH₄] = 0.1M. (c) Typical time dependence of the absorption of 4-NPA at 400 nm. (d) Plot of apparent rate constant (k_{app}) versus catalyst dose for 4-NPA reduction by NaBH₄ in the presence of Au@protein solution as catalyst. Conditions: [4-NP] = 5.5×10^{-5} M; [NaBH₄] = 0.1M.

catalytic activity of the Au nanoparticles for the reduction of 4-nitrophenolate in aqueous solution. Fig. 4b shows that after the addition of Au nanoparticles the absorption peak at 400 nm gradually drops with time. Fig. 4c shows the time dependence results obtained from the reaction conducted at room temperature. This observation indicates that after the addition of Au@protein bio-nanoconjugates, a certain period of time was required for the 4-nitrophenolate to adsorb onto the catalyst's surface before the reaction could be initiated. Here we define this period of time as the adsorption time or t_{ads} . After the adsorption time, the reaction becomes stationary and follows first order rate law. The apparent rate constant (k_{app}) is calculated from the linear slope of the curve.

3.1.2. Silver (Ag) nanoclusters (NCs) covalently conjugated to enzyme (CHT)^[18]

This study represents the synthesis of luminescent silver NCs of 1 nm average diameter using an enzyme, bovine pancreatic α -chymotrypsin (CHT). We obtain a well-dispersed, protein-conjugated silver NC that remained stable indefinitely in solution without any aggregation or deterioration of the spectral properties. The structural characterization of CHT-conjugated Ag NCs was done using steady-state UV – vis absorption/photoluminescence (PL) spectroscopy and high-resolution transmission electron microscopy (HRTEM). A comparative study on the enzymatic activity of the bio-nanoconjugates with the unbound enzyme, under similar experimental conditions, was also done. Picosecond-resolved Förster resonance energy transfer (FRET) from a fluorescent probe at the enzymatic active site to the Ag NC in the bio-nanoconjugates reveals the possible location of the metal cluster in CHT.

Synthesis of Ag-CHT bio-nanoconjugates

The typical procedure for the synthesis of conjugated Ag NCs is as follows: 10 mL of 100 μM CHT aqueous solution was prepared and dialyzed exhaustively against Millipore water at 4°C. This was carefully degassed with argon gas for 30 min. A freshly prepared AgNO_3 solution (100 mL of 100 μM) was then added to the above protein solution with vigorous stirring under an argon blanket. A degassed aqueous NaBH_4 solution (1 M) was then added to the above solution under vigorous stirring. The final molar ratio of BH_4^- : Ag^+ in the aqueous solution was maintained at 10:1. The reaction was allowed to proceed for 3 h, and the final solution was dialyzed against water exhaustively to remove

any excess of salts and NaBH_4 left in the solution. The final dialyzed solution was collected and stored at 4°C prior to analysis.

Figure 5 presents the HRTEM image of dialyzed sample of Ag-CHT bio-nanoconjugates at 100 K magnification which reveals a uniform size distribution of small spherical NCs. However, some of the aggregated clusters can also be seen in the TEM image, which are likely to have been formed in the original sample (*i.e.*, NC sample before dialysis) due to the presence of excess of NaBH_4 , which is known to induce aggregation of nanoparticles^[19]. A statistical analysis of ~200 small clusters (by hand) yields an average cluster size of ~1 nm and a standard deviation of 0.2 nm.

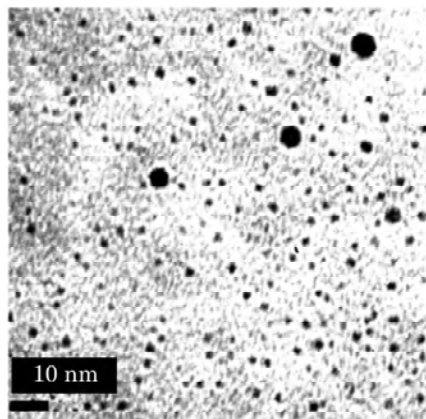


Fig. 5: High-resolution transmission electron micrograph (HRTEM) of dialyzed Ag-CHT bio-nanoconjugates.

Silver metal is known to have an intense plasmon absorption band in the visible region^[20]. Fig. 6 shows the UV – vis absorption spectrum of Ag-CHT conjugates, which reveals a surface plasmon band located at 413 nm. For the protein-bound Ag NCs, a prominent fluorescence is observed at ~680 nm when excited at 500 nm (Fig. 6). The size distribution of these silver nanoclusters was studied by exciting the nanoclusters at various excitation wavelengths (from 475 to 550 nm), which resulted in an insignificant shift in the emission maxima, suggesting a narrow size distribution.

Luminescent Ag-CHT bio-nanoconjugates exhibiting resonance energy transfer

The synthesized luminescent Ag nanocluster covalently attached to CHT at a site away from catalytic center of the enzyme. We demonstrated

that nontoxic Ag nanoclusters could work as an efficient energy acceptor in FRET studies on biomolecules. Here we used 4-nitrophenyl anthranilate (NPA, a fluorescent probe is known to bind at the enzymatic active site^[21]) as fluorescent energy donor.

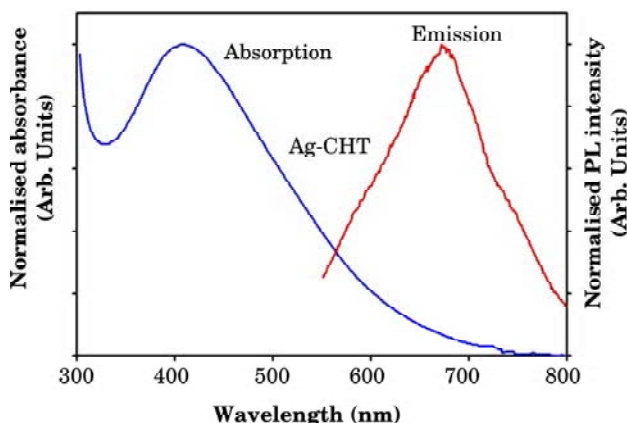


Fig. 6: Steady-state UV-vis absorption and photoluminescence (PL) spectra of Ag-CHT bio-nanoconjugates (excitation wavelength = 500 nm).

The huge overlap between NPA-CHT emission and the absorption of Ag-CHT nanocluster is expected to reveal inter-probe distance, when they are in a close proximity (Fig. 7).

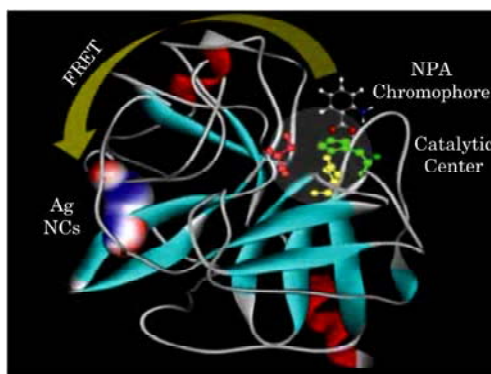


Fig. 7: Structure of α -chymotrypsin depicting the catalytic triad (His57, Asp102 and Ser195), NPA chromophore binding site and luminescent Ag nanocluster (covalently attached at a site away from catalytic center).

Figure 8a reveals the significant spectral overlap between NPA-CHT emission spectrum (donor, emission maximum at 428 nm) and Ag-CHT excitation spectrum (acceptor, excitation maximum at 413 nm) that favours the energy transfer from NPA to Ag in CHT. It has to be noted

that the absorption band of Ag–CHT bio-nanoconjugates remained same even after the reconstitution process. As revealed from Fig. 8b the overall steady–state emission intensity of the donor emission drastically decreased in the presence of acceptor. Also, the faster decay of donor in the presence of acceptor (Fig. 8c) as compared to that of the donor alone confirms the energy transfer from NPA to Ag cluster in CHT. The calculated donor to acceptor energy transfer efficiency from steady–state and time–resolved studies are 97.5% and 60.7% respectively. The estimated donor–acceptor distances from steady–state and time–resolved experiments are 19.1 and 32.6 Å, respectively.

3.1.3. Superparamagnetic fluorescent nickel (Ni)–enzyme bio-nanoconjugates^[22]

In the present work, we have synthesized, for the first time, luminescent and magnetic Ni NPs of 2.5 nm average diameters consisting of a single material instead of a composite nanoparticle system using an enzyme, bovine pancreatic α -chymotrypsin (CHT). We obtain well–dispersed, protein–nickel NPs that remain stable indefinitely in solution without any aggregation or deterioration of the spectral properties. The structural characterization of CHT encapsulated Ni NPs was done using steady–state UV–VIS absorption/photoluminescence (PL) spectroscopy and high resolution transmission electron microscopy (HRTEM). A comparative study on the enzymatic activity of the bio–nanoconjugates with the unbound enzyme, under similar experimental conditions, was also done. Picosecond–resolved FRET from a fluorescent probe at the enzymatic active site to the Ni NPs in the bio–nanoconjugates reveals the possible location of the metal cluster in CHT.

We also explored the possibility of using the FRET to monitor various temperature–induced unfolding states of the enzyme CHT. The synthesis methodology followed here is simpler compared to those of composite bifunctional NPs which may be extended further to Co, Fe etc. The combination of fluorescent and magnetic properties in one material would allow for visualization by fluorescence and manipulation in magnetic fields and could potentially be exploited for biomedical applications (*e.g.*, magnetic separation, immunoassays, stem cell tracking, and cancer metastasis monitoring using MRI, targeted drug delivery and hyperthermia cancer treatment).

Synthesis and characterization of Ni–CHT bio-nanoconjugates

To synthesize Ni–CHT bio–nanoconjugates we have used nickel (II) nitrate hexahydrate ($\text{Ni}(\text{NO}_3)_2 \cdot 6\text{H}_2\text{O}$) and employed similar

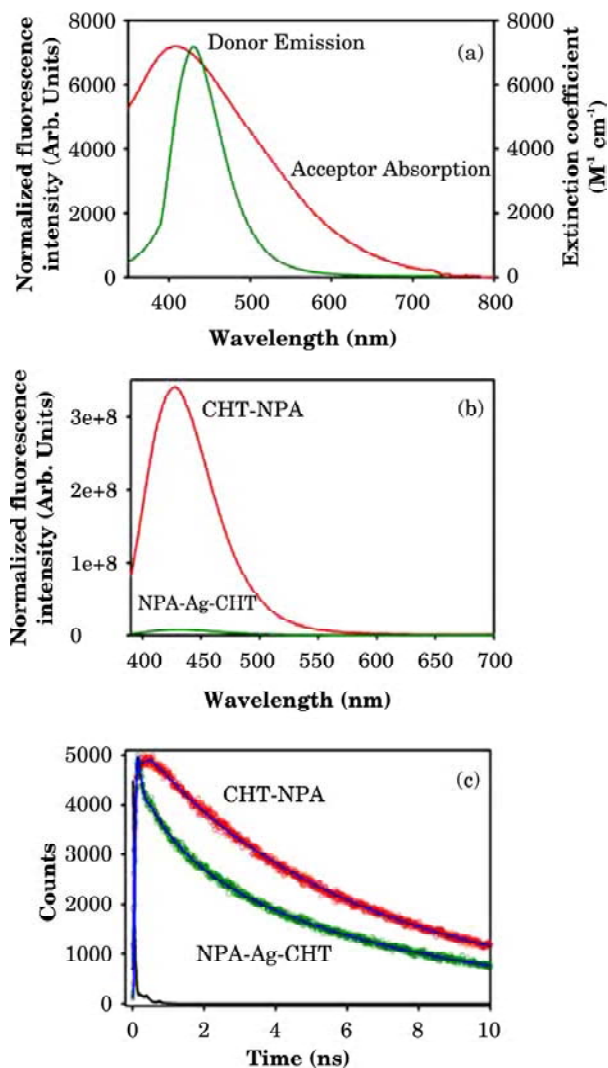


Fig. 8: (a) Spectral overlap between the donor (NPA-CHT) emission and acceptor (Ag-CHT) absorption. (b) Steady-state photoluminescence quenching of NPA-CHT (donor) in the presence of acceptor (Ag-CHT bio-nanoconjugates). The optical density of the samples at excitation and emission wavelengths was 0.05 and 0.07, respectively. (c) Picosecond-resolved fluorescence transients of donor (NPA-CHT) and donor-acceptor (NPA-Ag-CHT) complex.

procedure as we have followed during the synthesis of Ag-CHT bio-nanoconjugates^[18].

Figure 9a presents the TEM image of dialyzed sample of Ni-CHT bio-nanoconjugates. The images reveal that the bio-nanoconjugates are almost spherical in shape and follow a uniform size distribution. Particle

sizes have been estimated by fitting our experimental data measured from TEM image, with a log-normal size distribution. The size distribution is shown in inset of Fig. 9a. The average size of the Ni particles, as estimated from TEM image, has been found to be 2.5 nm. The corresponding HRTEM image (Fig. 9b) confirms the crystallinity of these NPs in their structure. The interplanar distance of fringes is measured to about 0.218 nm, corresponding to the distance between the (111) plane of nickel crystal lattice. Image in the inset of Fig. 9c represents the corresponding Fast Fourier Transform (FFT) pattern. A typical energy-dispersive X-ray (EDAX) spectrum of the dialyzed Ni-CHT sample is shown in the Fig. 9c and demonstrates the presence of Ni. Inset of Fig. 10b shows the UV-vis absorption spectrum of Ni-CHT

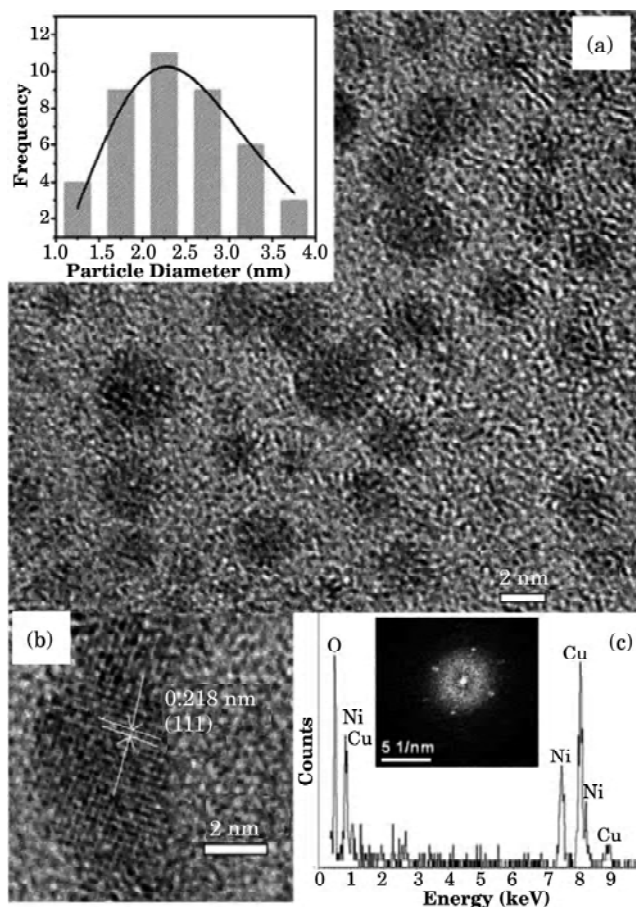


Fig. 9: (a) TEM image of as-prepared dialyzed Ni-CHT nanobiocomjugates. The size distributions of the samples are shown in the inset. (b) A HRTEM image showing the crystalline structure of Ni NPs. (c) EDAX spectrum of the Ni NPs. FFT image of the Ni-CHT bio-nanoconjugates is shown in the inset.

conjugates, which reveals a surface plasmon band located at 417 nm. On the basis of Mie theory²³ and its generalized versions^[24,25], information concerning Ni nanoparticle sizes can be derived from the analysis of the absorption band. The Ni NPs exhibited fluorescence in the visible region as shown in Fig. 10a. The photoluminescence of the nanoparticles arises due to their molecule-like electronic structure.

The emission originates probably from the recombination of the excited electrons from excited states in the sp band with the holes in the low-lying d band (interband transition). Fluorescence decay of Ni NPs was measured. Data obtained using a picosecond-resolved time-correlated single-photon counting (TCSPC) technique is shown in Fig. 10b. Lifetime values of the NP were obtained by the numerical fitting of the fluorescence at 500 nm. They are 0.12 ns (54.3%), 1.17 ns (17.4%) and 4.34 ns (28.3%). The overall PL decay leads to an average life time value of 1.49 ns. It is important to note that the excitation spectra of Ni NPs shows peak centered at 320 nm and 360 nm (Fig. 10a). So, the

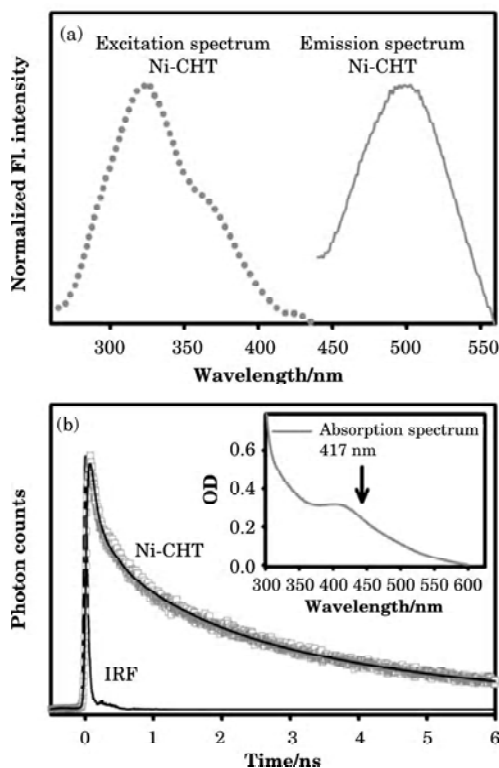


Fig. 10: (a) Excitation and emission spectra of Ni -CHT bio-nanoconjugate (b) Fluorescence decay of the same ($\lambda_{\text{ex}}=375 \text{ \AA}$) monitored at 500 nm. Absorbance spectra of Ni-CHT bio-nanoconjugates is shown in the inset. IRF stands for instrument response function.

conclusion is that the SPR peak centered at 417 nm is not responsible for the luminescence. It has been demonstrated previously^[26] for spherical NPs that the broadening of the plasmon with decreasing size in the quantum size regime, $d < 3$ nm, in the case of both Au and Ag is rapid and increases the absorbance of both UV and NIR regions relative to the plasmon peak, whose height decreases. It is in fact well established that the surface plasmon bandwidth is inversely proportional to the radius r of the particle for sizes smaller than about 20 nm^[27]. The increased broadening with decreasing size enhances both the low- and high-energy absorbance of the smallest clusters, causing the plasmon to be completely damped below a size of $d = 2.2$ nm for Au but still observable at the size of $d = 1.55$ nm for Ag^[26]. In our case the emitting Ni-CHT bio-nanoconjugate are smaller than the 2.5 nm and their SPR is not observable in the absorbance spectra due to broadening as explained above.

Magnetic properties were studied by using standard zero-field-cooling (ZFC) and field-cooling (FC) procedures and field-dependent magnetization measurements. Measurements of the ZFC, FC magnetization as a function of temperature was performed between 5 K and 300 K under an applied field of 100 Oe and the results are shown in Fig. 11a. The ZFC/FC curve evidences a superparamagnetic behavior above the blocking temperature $T_B = 13.2$ K (Fig. 11b and c).

Structure and functional characterization of luminescent Ni-CHT bio-nanoconjugates

It is well-known that the sodium borohydride induces cleavage of disulfide bonds to sulfhydryl groups in a protein and perhaps breaks some of the peptide bonds also leading to its denaturation. Reconstitution of a protein denotes the process of returning of a denatured protein to its original structure and activity. In our experiment, CHT and Ni-CHT conjugates were reconstituted by dialyzing each of them separately against water of pH = 8.0–8.5 for 24 h in aerated conditions. Fig. 12 compares the CD spectra of reconstituted CHT, and reconstituted Ni-CHT solutions. Native CHT displays CD features with minima at 202 and 232 nm, corresponding to the native secondary and tertiary structure of the protein^[28,29], respectively. It is found that there is a slight loss of tertiary structure in the CD spectrum at 232 nm and ~ 3 nm shift of the minimum at 202 nm for both reconstituted CHT as well as reconstituted Ni-CHT samples compared to the native CHT. Quantification of the CD data through curve-fitting analysis revealed that the conformation of the reconstituted Ni-CHT (19% helix) was identical to that of the reconstituted CHT (19% helix), demonstrating a small perturbation of the native structure of the protein (24% helix).

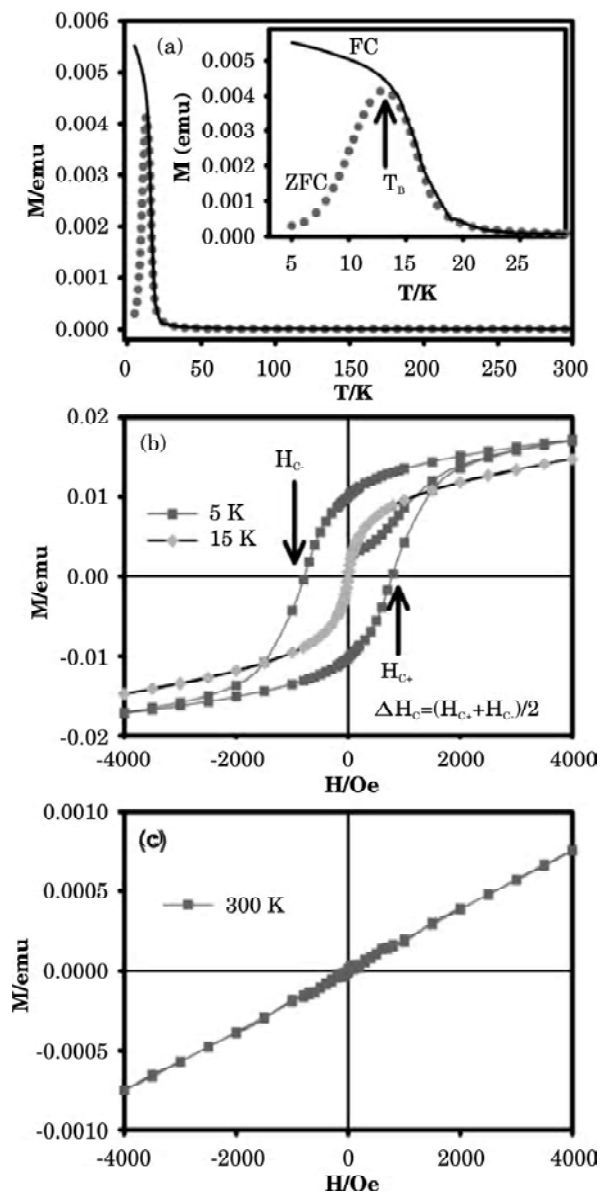


Fig. 11: (a) ZFC and FC magnetization as a function of temperature measured at an applied field of 100 Oe for the Ni-CHT bio-nanoconjugates. Inset: An expanded view of the plot, clearly showing T_B . (b) M-H plots of Ni NPs at 5 K (symbol: square) and 15 K (symbol: triangle) (c) M-H plot at 300 K of the Ni NPs.

To prove that the Ni-bound CHT are still functional, we also carried out the enzymatic activities of Ni-CHT and the results are shown in the inset of Fig. 12. We find that the specific activity (in units/mg) of

the reconstituted Ni-CHT complex was retarded by 2 times compared to that of reconstituted CHT consistent with our previous studies^[30,31] on analogous systems (CdS-bound CHT and Ag-bound CHT). Our observation also closely matches with the enzymatic activities performed by Jordan *et al.*^[29] for a similar system (CHT-Au-TCOOH; Au-TCOOH being the gold-nanoparticle-capped tetra(ethylene glycol) carboxylate ligands) where they observed a 3-fold decrease in the rate of CHT complexed with AuTCOOH compared to CHT alone. The above experimental observations may indicate that the nucleation and the subsequent growth of Ni NPs in CHT could possibly take place at a site that is away from the enzymatic active site of CHT. It has to be noted that the attachment of 2.5 nm diameter NP to the active site of the enzyme is expected to act as an inhibitor of CHT activity on the substrate AAF-AMC (1–2 nm diameter) resulting in retardation of the enzymatic activity by several orders of magnitude^[32]. However, the moderate retardation in the enzymatic activity of Ni-CHT complex as compared to CHT alone could be the manifestation of the dynamical rigidity of CHT upon attachment of a Ni NP.

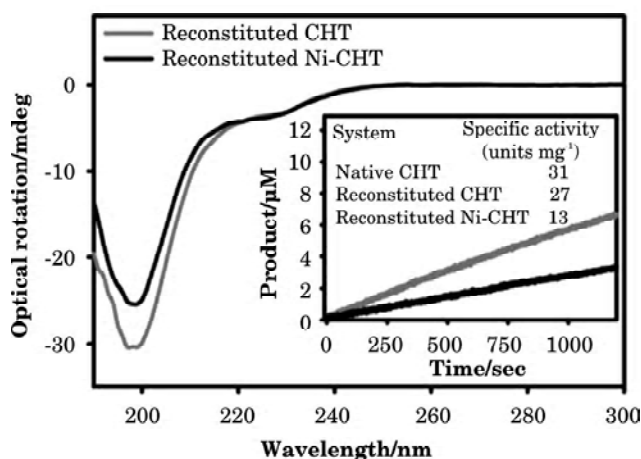


Fig. 12: CD spectra of reconstituted CHT and reconstituted Ni-CHT bio-nanoconjugates. Enzymatic activities of CHT and reconstituted Ni-CHT bio-nanoconjugates on the substrate, AAF-AMC.

3.1.4. Copper quantum clusters in protein matrix^[33]

The synthesis of Cu QCs by a simple one-pot chemical reduction method by using a commercially available protein, bovine serum albumin (BSA) has been established. It has been demonstrated that BSA can be used as the model protein for the synthesis and stabilization of gold nanoclusters^[34]. The resulting Cu QCs were highly resistant to oxidation

and exhibits photoluminescence and highly stable properties in a colloidal dispersion. The as prepared blue emitting clusters were assigned a molecular formula based on MALDI-MS. The as synthesised quantum clusters were characterized thoroughly using various spectroscopic and microscopic techniques (UV-vis, luminescence, TEM, DLS, XPS, MALDI-TOF, TGA, and DSC). The effect of oxidizing agent on the luminescence property of the cluster solution was probed. The luminescence of the QCs was exploited as a selective sensor for the detection of the toxic Pb^{2+} ion. The reason of quenching was found to be aggregation manifested as revealed from our DLS study.

Synthesis and characterization of $\text{Cu}_{\text{QC}}@\text{BSA}$ bio-nanoconjugates

In a typical experiment, aqueous CuSO_4 solution (1 mL, 20 mM) was added to BSA solution (5 mL, 15 mg/mL). The solution was stirred at room temperature for 2–3 min and then NaOH solution was introduced so that pH 12 is achieved. The color of the solution changed from blue to violet within 2–5 min. Finally, the mixture was allowed to stir for 6 to 8 h at 55°C and the colour changes to light brown. It has to be noted that formation of the Cu QCs at room temperature is possible; however, need more time (48 h) compared to that at 55°C (6–8 h). It is crucial to know the key parameters such as concentration, pH and temperature to obtain a high concentration of Cu QCs. Hence, a series of control experiments have been performed and these results indicate that luminescence intensity was high for the reaction with 20 mM CuSO_4 solution at pH ~ 12. We have used these pH and concentration for synthesizing larger amounts of clusters.

Although weak as compared to the 280 nm peak of pure BSA, a clear absorption spectrum at 325 nm appears in the final solution (Fig. 13a). In order to realize the origin of 325 nm peak, we have taken into account any kind of oxidation product of the amino acids in protein. However, it is well known that, all the aromatic amino acids have a characteristic absorption peak ≤ 280 nm and a few tryptophan metabolites like kynurenine, 3-hydroxykynurenine, N-formylkynurenine have an absorption peak above 300 nm. Our earlier extensive studies confirmed that kynurenine^[35] and its derivatives^[36] in proteins have a distinct UV-vis peak at above 350 nm. The observed 325 nm absorption peak as well as the emission maxima (see below) revealed in the present study clearly rules out the possibility of any tryptophan metabolites rather the formation of a new type of material in the protein environment. The high-resolution transmission electron microscopy (HR-TEM) images (Inset of Fig. 13a) showed that the average size is 2.8 ± 0.5 nm where the crystal lattice fringes are 2.02 Å apart which indicates the (111)

planes of the metallic Cu. This is not surprising because clusters may fuse to form crystals in presence of strong electron beam irradiation^[37]. Swelling of the protein size as revealed from dynamic light scattering (DLS) measurement indicates the formation of new species inside the protein having size about ~3 nm. Protein fragmentation as well as enhancement of aggregation is also shown in Fig 13B. Recently, it has been reported that fragmentation of protein can occur when pH of the environment changes drastically^[38]. It is also well established that protein coordinates with copper ion to form aggregates^[39].

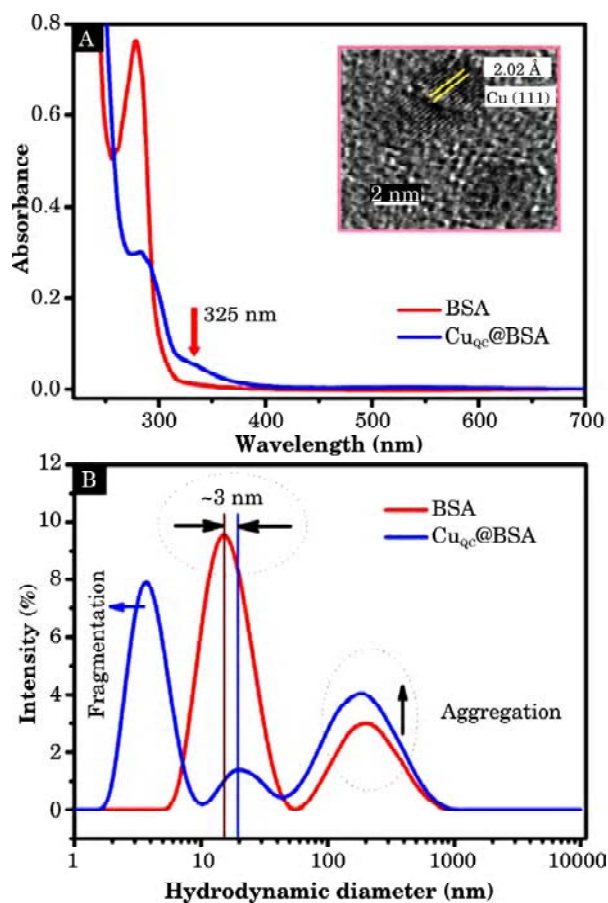


Fig. 13: (a) UV-vis absorption spectra of BSA (red line) and Cu_{QC}@BSA solution (blue line). Inset. HRTEM of Cu QCs after being exposed to the electron beam. (b) DLS spectra of BSA (red) and Cu_{QC}@BSA (blue). All the parameters are same in both cases.

XPS analysis is carried out to determine the oxidation state of copper in the samples. Two intense peaks are observed at 932.3 and 952.0 eV (Fig. 14b), which are assigned to 2p_{3/2} and 2p_{1/2} features of Cu (0). As–

synthesized material has also been studied using matrix-assisted laser desorption/ionization time of flight (MALDI-TOF) mass spectrometry to understand the number of copper atoms in the cluster core. The mass spectrum of BSA showed a major peak at around 66.4 Da due to the mono-cation, which agrees with previous results on Ag_{15} clusters^[40] (Fig. 14c, Inset 1). Cu cluster containing BSA showed two distinct, but low intensity peaks at m/z 66 723 and 67 228 kDa besides the parent protein peak. The difference between the above peaks with the host protein spectrum measured at pH 12 may be attributed to the 5 and 13 copper atoms respectively; we assign the clusters to be Cu_5 and Cu_{13} .

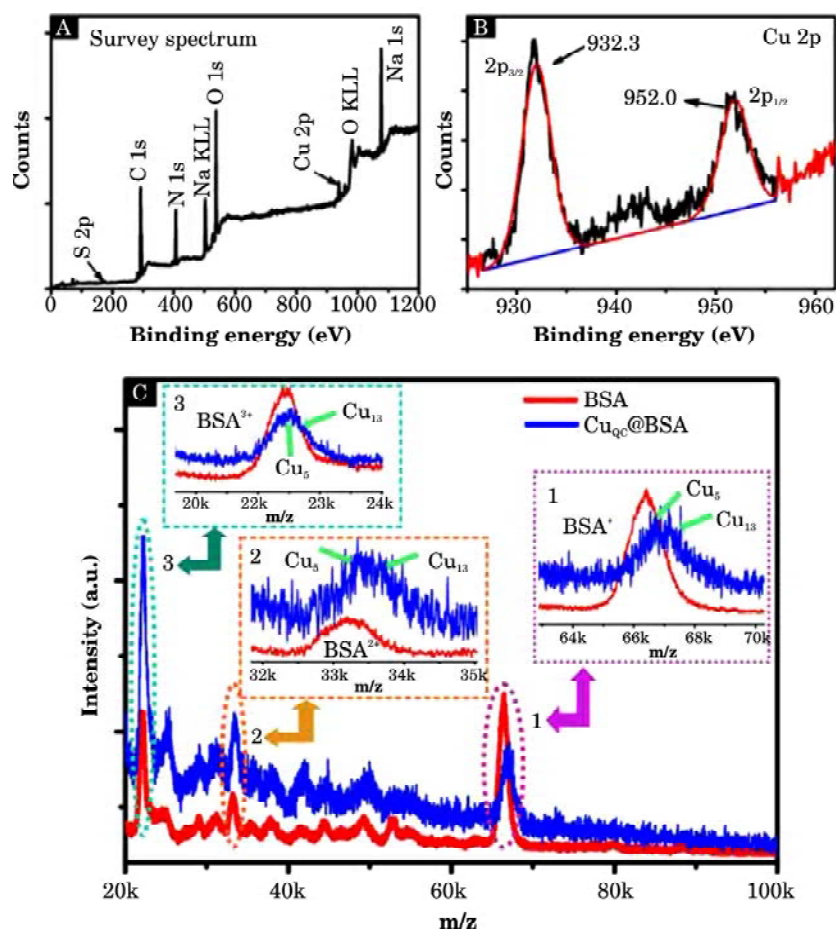


Fig. 14: (a) XPS survey spectrum of $\text{Cu}_{\text{QC}}@BSA$ (black). (b) XPS spectrum in the Cu 2p region of $\text{Cu}_{\text{QC}}@BSA$. (c) MALDI-TOF mass spectra of BSA (red) and $\text{Cu}_{\text{QC}}@BSA$ (blue). The peaks due to singly, doubly and triply charged ions of $\text{Cu}_{\text{QC}}@BSA$ are expanded in the inset.

The luminescence of $\text{Cu}_{\text{QC}}\text{@BSA}$ revealing distinct excitation and emission maxima at 325 and 410 nm, respectively is evident from Fig. 15a. The peak position (325 nm) of the excitation spectrum is almost alike to the Cu QCs absorption band in Fig. 13A. Protein alone shows insignificant emission upon 325 nm excitation at pH 12 confirming the absence of emitting amino acid metabolites. The luminescence decay of the $\text{Cu}_{\text{QC}}\text{@BSA}$ in water is measured by a picosecond-resolved time-correlated single-photon counting (TCSPC) technique (Inset of Fig. 15b). The decay profile of the $\text{Cu}_{\text{QC}}\text{@BSA}$ is monitored at an excitation wavelength of 300 nm. The numerical fitting of the luminescence

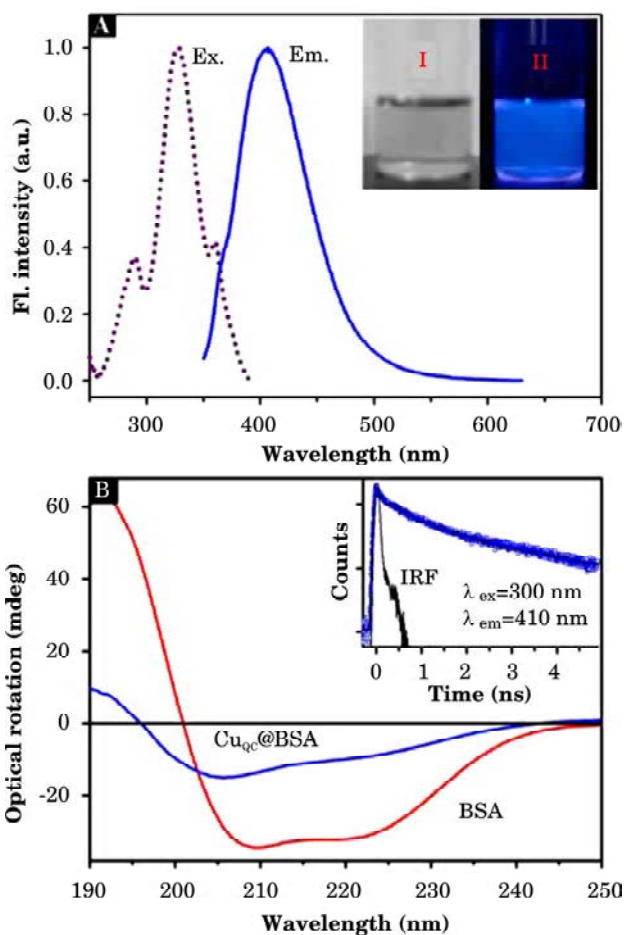


Fig. 15: (a) Excitation and emission spectra of $\text{Cu}_{\text{QC}}\text{@BSA}$ at room temperature (pink and blue line). Inset contains the photographs of the $\text{Cu}_{\text{QC}}\text{@BSA}$ under visible light (I) and under UV light (II). (b) Far-UV circular dichroism (CD) spectra of BSA (red) and $\text{Cu}_{\text{QC}}\text{@BSA}$ (blue). Inset. Photoluminescence decay of $\text{Cu}_{\text{QC}}\text{@BSA}$ with instrument response function (IRF) ~ 60 ps. Standard error of decay time components are $\sim 5\%$.

collected at 410 nm reveals time constants of 0.03 ns (78%), 0.71 ns (15%) and 3.5 ns (7%), which may be due to the electronic transitions between “sp” conduction band and filled “d¹⁰” band.

Toxic metal ion sensing application of Cu_{QC}@BSA bio-nano-conjugates

The luminescence of the as-prepared Cu_{QC}@BSA can be used as a highly sensitive and selective luminescence “turn-off” sensor for the Pb²⁺ ion. We found that the luminescence of Cu QCs is quenched in the presence of Pb²⁺ ion. It can be seen from the Fig. 16a that more and more quenching occurs with an increase in Pb²⁺ ion. Herein, we have also carried out studies with other metal ions, such as Hg²⁺, Ca²⁺, Co²⁺, Zn²⁺, Ni²⁺, Cd²⁺, Mg²⁺, Na⁺, and K⁺ under exactly similar conditions that were used for the detection of Pb²⁺ ion. Chlorides and nitrates of the metals are used. Metal ions are added to aqueous solutions of the Cu QCs such that the final concentration was 200 ppm and the luminescence of the Cu QCs is measured immediately after the addition of ions. However, no such quenching effect like that of the Pb²⁺ ion is observed. The relative luminescence quenching of Cu_{QC}@BSA toward various common metal ions is presented in Fig 16b. This result suggests that our luminescent Cu QCs are selective for Pb²⁺ detection. The luminescence quenching in the presence of Pb²⁺ can be attributed to the QC aggregation induced by the complexation between BSA and the Pb²⁺ ion. BSA contains a high-affinity site for Pb²⁺ ion; the binding involves carboxylate groups. To explore the quenching mechanism, we have performed DLS measurement. It can be seen from Fig. 16C that only Pb²⁺ ion can induce the protein-protein interaction which leads to spherical aggregation of Cu_{QC}@BSA. We have also checked the efficacy of Pb²⁺ ion detection in presence of other metal ions (Hg²⁺, Ca²⁺, Co²⁺, Zn²⁺, Ni²⁺, Cd²⁺, Mg²⁺, Na⁺, and K⁺) of similar concentrations.

3.2. Metal Oxide-Based Nanobiomaterials

3.2.1. Fabrication of manganite nanoparticles towards advanced nanobiomaterials^[41]

Herein, we report the functionalization of one of the most promising manganite nanoparticles (NPs), La_{0.67}Sr_{0.33}MnO₃ (called LSMO hereafter) with biocompatible citrate ligand. The size selective solubilization of the functionalized NPs in aqueous solution has also been demonstrated from HRTEM. The UV-vis spectroscopic study on the functionalized NPs shows an intense peak at visible region as a consequence of electronic interaction of the citrate ligand with the surface atoms of the

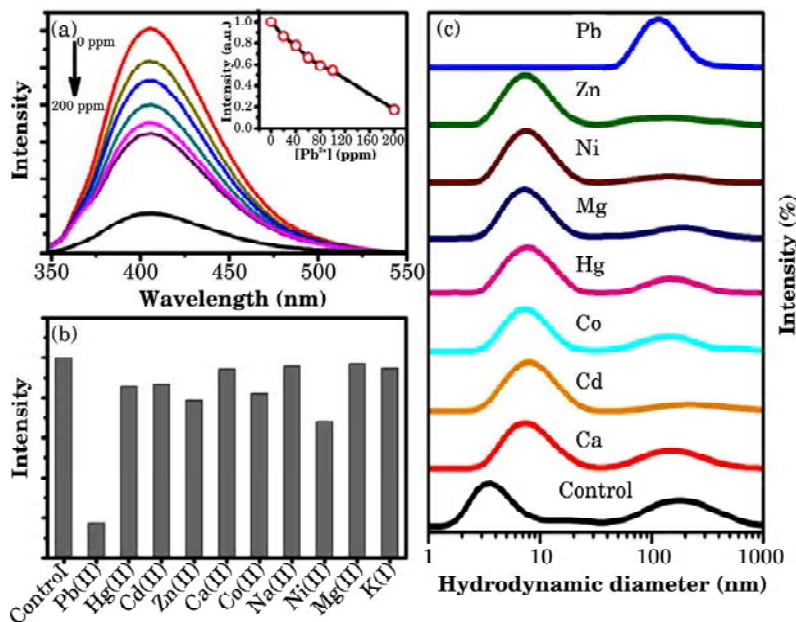
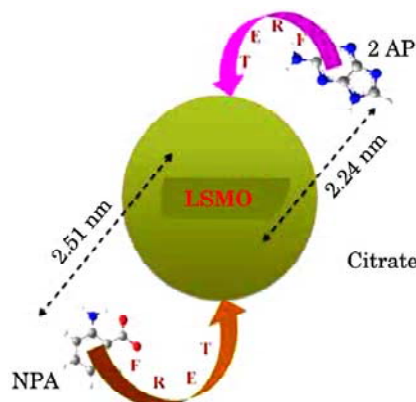


Fig. 16: (a) Luminescence responses of $\text{Cu}_{\text{QC}}\text{@BSA}$ after the addition of Pb^{2+} ion (0–200 ppm). Inset: Plot of the luminescence peak intensity versus the concentration of Pb^{2+} ion. (b) Selectivity of the $\text{Cu}_{\text{QC}}\text{@BSA}$ to different metal ions. The Luminescence intensities were recorded at 406 nm. For panel B, the final metal ion concentrations are 200 ppm. (c) DLS spectra of $\text{Cu}_{\text{QC}}\text{@BSA}$ solution in absence (control) and presence of different metal ions.

NPs. In our studies we have exploited the visible band of the functionalized NPs in order to study the interaction of the NPs with small biologically relevant ligands namely 2–Aminopurine (2AP) and 4–Nitrophenyl anthranilate (NPA). FRET of a covalently attached probe 4–Nitrophenyl anthranilate (NPA) with the capped NPs confirm the attachment of the NPA ligands with the surface functional group (–OH) of the citrate ligand. The FRET of a DNA base mimic, 2–Aminopurine (2AP), with the NPs confirms the surface adsorption of 2AP. The FRET distances from the attached ligand to the host LSMO NPs also confirm the existence of the isolated functionalized NPs in the aqueous solution.

Functionalization of LSMO nanoparticles

We have synthesized the bulk LSMO nanoparticles following a reported procedure where a modified sol–gel technique has been designed especially for the preparation of complex oxide nanoparticles. The as prepared LSMO nanoparticles were rendered water–soluble using the



Scheme 1: Functionalization of the manganite nanoparticles (NPs) with citrate ligands is shown. Covalent attachment of the fluorescent probe NPA and non-covalent adduction of one of DNA base mimics 2AP are also shown. The efficient energy transfer (FRET) from the fluorescent ligands to the NPs and corresponding donor-acceptor distances are also indicated.

reactivity of carboxylate group of citrate with the Mn centre in LSMO, by three hours of extensive mixing using the cyclo-mixer. The unreacted NPs were filtered out and a resulting greenish-yellow solution was obtained, indicating successful functionalization.

To obtain direct evidence for the functionalization of LSMO NPs, FTIR measurements were performed on both the as-prepared and functionalized samples. The FTIR spectra of LSMO NPs, Citrate-LSMO conjugates and tri-sodium citrate were shown in Fig. 17a. From FTIR study it is evident that the COO^- functional group/groups present in citrate, covalently bonded to the NPs surface and the remaining polar functional groups make the NPs water soluble. Moreover, as evident from Fig. 17b the UV-vis spectrum of the citrate capped LSMO represents a high intensity broad band centred at 430 nm along with a smaller band centred at 742 nm.

Figure 18a represents the TEM image of the solubilized Citrate-LSMO NPs. The image reveals that the solubilized NPs are almost spherical in shape and follow a uniform size distribution. The average sizes of the solubilized NPs are estimated from the TEM image has been found to be 2.6 nm. The corresponding HRTEM image (upper inset of Fig. 18a) confirms the crystallinity of the NPs in their structure. The interplanar distance of the fringes is measured to be about 0.29 nm, corresponding to the distance between (104) planes of the LSMO crystal lattice. The selective area electron diffraction (SAED) pattern simultaneously obtained from the TEM measurements (lower inset of Fig. 18a) suggests single crystalline structure of Citrate-LSMO NPs.

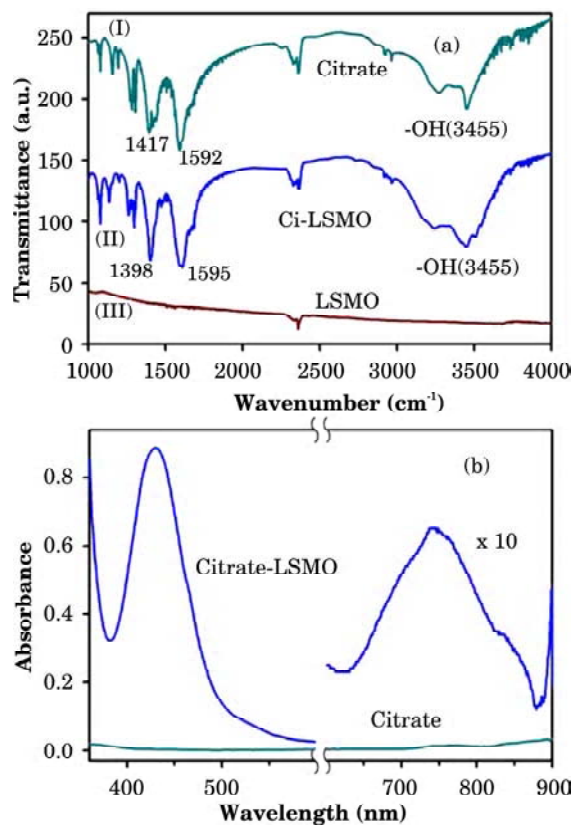


Fig. 17: (a) shows FTIR spectra of (I) pure tri-sodium citrate crystals, (II) functionalized Citrate-LSMO and (III) as-prepared bulk LSMO, recorded with a KBr pellet. (b) shows UV-vis spectra of citrate functionalized LSMO NPs in solution.

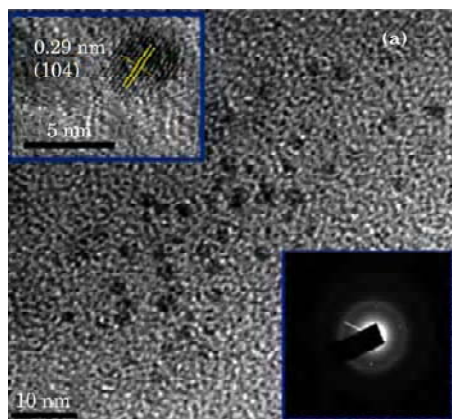


Fig. 18: (a) TEM image of Citrate-LSMO NPs, upper inset shows a HRTEM image of the crystalline structure of Citrate-LSMO NPs, lower inset shows the selective area electron diffraction (SAED) pattern of the Citrate-LSMO NPs.

Further conjugation of biomolecules with the functionalized Citrate-LSMO NPs

The direct bonding of citrate ligands to the LSMO NPs surfaces ensured that the overall size of the NPs remained small with a thin solubilizing shell. The $-OH$ and $-COO^-$ functional groups of Citrate-LSMO were labelled covalently with 4-Nitrophenyl anthranilate (NPA) chromophore⁴² and non-covalently with 2AP, respectively. In both cases an efficient FRET occurs (Fig 19 and 20) between the donor (Citrate-NPA, Citrate-2AP) and acceptor (Citrate-LSMO NPs). The overall picture that is revealed from our studies is schematically shown in Scheme 1.

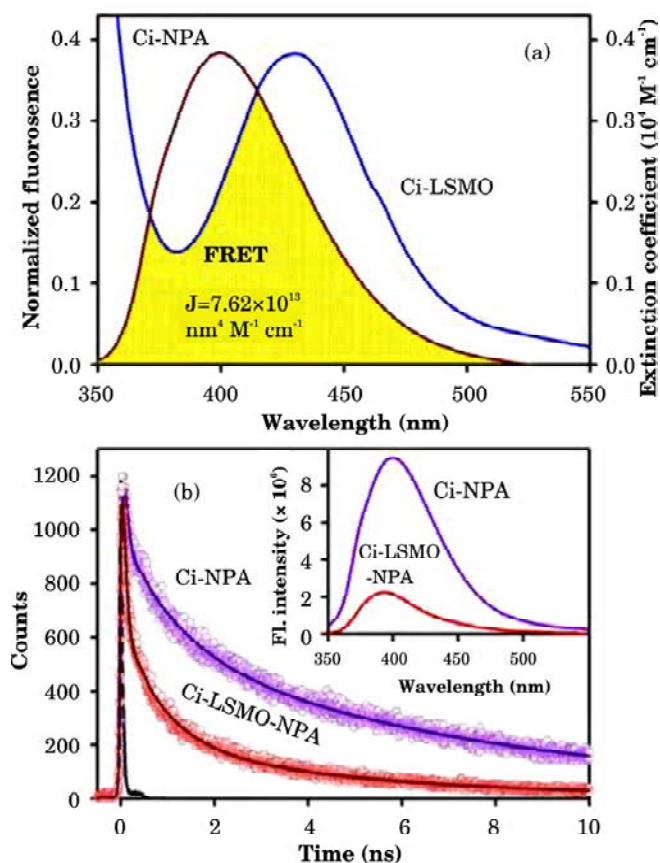


Fig. 19: (a) shows the spectral overlap between donor (Citrate-NPA) emission and acceptor (Citrate-LSMO) absorption, (b) shows quenching of the donors excitation lifetime in the presence of the acceptor, inset shows steady-state quenching of the donor emission. Excitation wavelength of 320 nm and 375 nm is used for steady - state and time resolved experiments respectively.

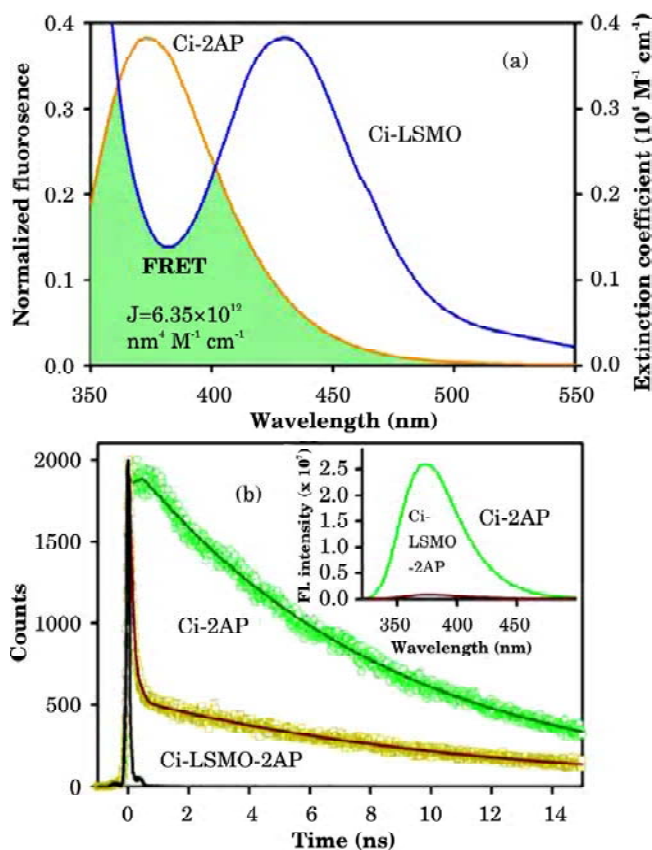


Fig. 20: (a) shows the spectral overlap between donor (Citrate–2AP) emission and acceptor (Citrate–LSMO) absorption, (b) shows quenching of the donors excitation lifetime in the presence of the acceptor, inset shows steady – state quenching of the donor emission. Excitation wavelength of 300 nm is used for both the experiments.

3.2.2. Emergence of multicolor photoluminescence in $\text{La}_{0.67}\text{Sr}_{0.33}\text{MnO}_3$ (LSMO) nanoparticles upon biomolecular functionalization

Herein, we report the emergence of multicolor photoluminescence in a mixed valence manganite nanoparticle $\text{La}_{0.67}\text{Sr}_{0.33}\text{MnO}_3$ (LSMO NP), achieved through electronic structural modification of the nanoparticles upon functionalization with a biocompatible organic ligand, sodium tartrate. From UV–vis absorption, X–ray photoelectron spectroscopy (XPS), time–resolved photoluminescence study and Raman spectroscopic measurements it is revealed that ligand–to–metal charge transfer transitions from highest occupied molecular orbital (HOMO, centered

in tartrate ligand) to lowest unoccupied molecular orbital (LUMO, centered in $\text{Mn}^{3+/4+}$ of the NPs), and d–d transitions involving Jahn–Teller sensitive Mn^{3+} ions in the NPs plays the central role behind the origin of multiple photoluminescence from the ligand functionalized LSMO NPs.

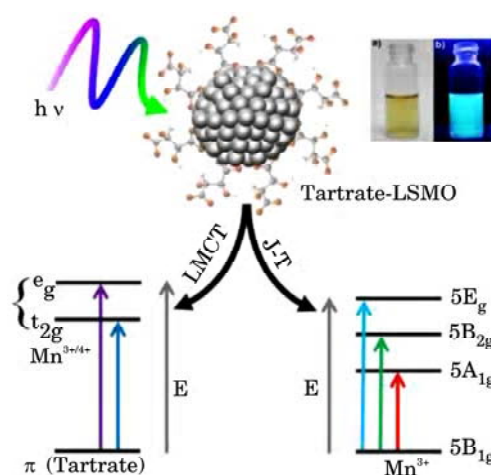


Fig. 21: Schematic presentation of the most likely events occurring when a photon hits a tartrate functionalized LSMO NPs (T-LSMO): ligand-to-metal charge transfer transitions from HOMO (centered in tartrate ligand) to LUMO (centered in $\text{Mn}^{3+/4+}$ of the NP), and d–d transitions involving Jahn–Teller sensitive Mn^{3+} ions in the NP. Arrows show the transition involved upon excitation by photon of different energy. Inset shows the photographs of T-LSMO NPs under visible light (a) and under UV light (b).

Preparation of photoluminescent LSMO NPs

We have solubilized the as prepared LSMO NPs into water by using the reactivity of hydroxyl ($-\text{OH}$) and carboxylate (COO^-) groups of tartrate. First, we prepared 6 mL of 0.5 M tartrate solution (pH~7) and then 200 mg as prepared LSMO NPs was added to the solution followed by 6 hours of extensive mixing by cyclo-mixer. Finally the non-functionalized bigger sized NPs were filtered out (by a syringe filter of 0.22 mm diameter) and UV vis optical absorption of the resulting greenish–yellow filtrate solution was measured.

Next, we increased the pH of the resulting greenish–yellow Tartrate-LSMO solution from pH~7 to pH~12, by drop wise addition of NaOH. The greenish–yellow color of the solution turns to yellowish–brown and the resulting solution was heated at 70°C under vigorous stirring condition for 8 hours. After eight hours the solution became highly fluorescent.

Characterization of tartrate functionalized LSMO NPs

Figure 22a illustrates the UV-vis absorption spectrum of as-prepared LSMO, tartrate and T-LSMO NPs (at pH ~ 7). In case of T-LSMO, it shows two peaks at 300 and 440 nm, a shoulder descending into lower energies around 580 nm and a broad band at 758 nm. The peak at 300 nm could be assigned to one of the possible high energy charge-transfer, ligand-to-metal charge transfer (LMCT) processes involving tartrate-Mn^{3+/4+} interaction^[43]. The other expected LMCT band^[43] at around 385 nm has not been observed in the absorption spectrum presumably because the band has been masked by the more intense 300 nm absorption, however, is distinctly visible in the excitation spectrum at around 372 nm (Fig. 22b). Other bands at 440, 580 and 758 nm are reasonably attributed to d-d transitions of Mn³⁺ in T-LSMO NPs, as the degeneracy of 5E_g ground state term of d⁴ (Mn³⁺) high-spin octahedral environment, has been lifted by the Jahn-Teller effect, that ultimately leads to a tentative assignment of the observed bands to the transitions 5B_{1g} → 5E_g, 5B_{1g} → 5B_{2g} and 5B_{1g} → 5A_{1g}, respectively^{44,45} (Fig. 21). Reflection of the UV-vis absorption patterns into the photoluminescence excitation spectra (shown in Fig. 22b) of the sample has been expected and indeed observed. Which further supports the assignment of the electronic excited states those give rise to multicolour photoluminescence.

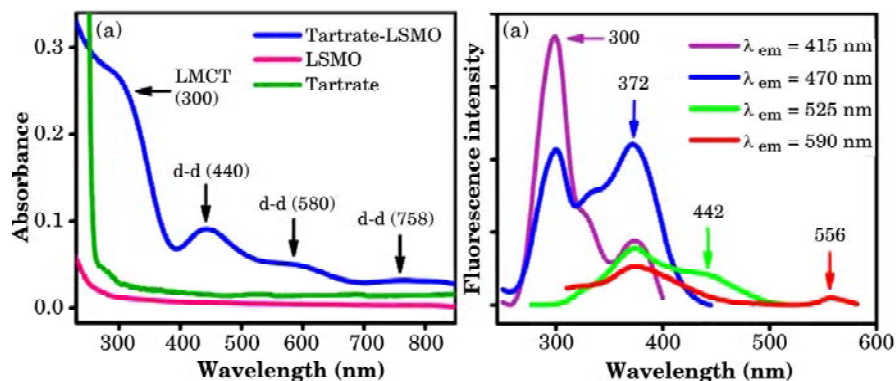


Fig. 22: (a) UV vis absorption spectrum of as-prepared LSMO, tartrate and tartrate-LSMO NPs (in aqueous solution at pH~7). (b) Photoluminescence excitation spectra of tartrate-LSMO NPs at different emission maximum (shown in Fig. 23a) of 415, 470, 525 and 590 nm.

Figure 23a displays the normalized photoluminescence spectra of T-LSMO NPs at room temperature. The four distinct emission bands starting from blue to red region (maximum at 418, 470, 520 and 590 nm) of the spectrum, corresponding with four distinct excitation

wavelengths (300, 375, 425 and 570 nm) are clearly observed. The photoluminescence as shown in Fig. 23a may be assigned to originate predominantly from the LMCT [tartrate \rightarrow Mn^{3+/4+}] excited states and ligand field excited states of the metal (Mn³⁺) d orbitals. Photoluminescence from either an intraligand or metal to ligand charge-transfer (MLCT) excited states are considered unlikely. Photoluminescence quantum yields (QY) of the T-LSMO NPs at pH~12, were obtained by using the comparative method of Williams *et al.*^[46], which involves the use of well characterized standard samples with known QY values. Photoluminescence QY of 1×10^{-2} (for 415 nm PL), 4×10^{-3} (for 470 nm PL), 8×10^{-4} (for 520 nm PL) and 2.4×10^{-4} (for 590 nm PL) were obtained relative to the standards 2-amino-purine (2AP), 42, 6-diamidino-2-phenylindole (DAPI), Hoechst (H33258) and ethidium bromide (EtBr), respectively.

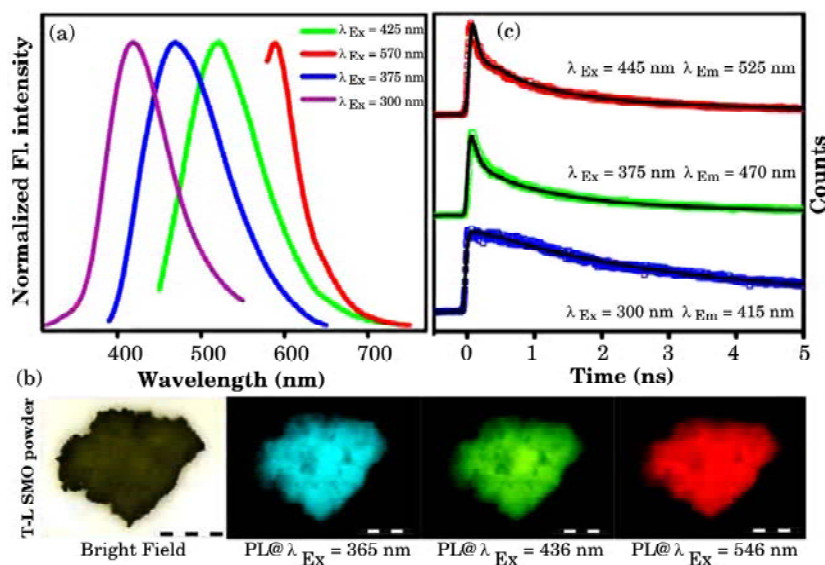


Fig. 23: a) Normalized steady-state photoluminescence spectra collected from tartrate-LSMO NPs with four different excitation wavelengths of 300, 375, 425 and 570 nm at pH~7. b) Fluorescence microscopic images of tartrate-LSMO NPs powder under irradiation of white light (bright field) and light of three different wavelengths of 365, 436 and 546 nm. Scale bars in the figure are of 500 μ m. c) Picosecond-resolved photoluminescence decays transients of tartrate-LSMO NPs in water measured at emission wavelengths of 415, 470 and 525 nm upon excitation with laser source of 300, 375 and 445 nm wavelengths respectively.

Further insights into the nature of the photoluminescence can be obtained by analyzing the luminescence lifetime decay transients of T-

LSMO NPs in water, measured by picosecond-resolved time-correlated single-photon counting (TCSPC) technique. Fig. 23c shows the luminescence lifetime decay transients of the water soluble NPs at three different emission wavelengths (415, 470 and 525 nm) corresponding with three different laser excitation wavelengths (300, 375 and 445 nm) respectively. Although the origin of 415 and 470 nm emission is from the LMCT excited states, luminescence lifetime of 415 nm emission is much longer ($\langle\tau\rangle = 4.77$ ns) than the 470 nm ($\langle\tau\rangle = 0.84$ ns) emission. Substantial shortening in the luminescence lifetime of 470 nm emission and its close resemblance with the 525 nm emission lifetime ($\langle\tau\rangle = 0.64$ ns, originates from ligand field excited states of the metal d orbital's) presumably due to enhanced radiative deactivation of the excited state by the close proximity with metal d-d states^[47].

In order to get supporting evidence regarding the origin of different optical properties of T-LSMO NPs, XPS, Raman and FTIR analysis have been carried out for LSMO NPs, before (as prepared NPs) and after (T-LSMO) functionalization with sodium tartrate. From XPS study it is observed that, upon functionalization with tartrate a partial reduction of Mn^{3+} and Mn^{4+} centers in the NPs occur and resulting the formation of Mn^{2+} ions, whereas, La^{3+} and Sr^{2+} centers remains unaffected. Through Raman spectroscopic investigation we have observed a perturbation of $\text{Mn}^{3+}\text{-O-Mn}^{4+}$ bond. As shown in Fig. 24a, between the two characteristic peaks of LSMO NPs at 436 and 636 cm^{-1} (corresponding with A_{1g} -like and B_{1g} -like vibrational modes involving Mn-O stretching vibration modes of MnO_6 unit, respectively)⁴⁸, peak around 436 cm^{-1} completely disappeared and the 636 cm^{-1} peak becomes broadened (possibly due to mixing of tartrate features) after their functionalization with tartrate. This disappearance of A_{1g} -like stretching vibration mode that represents the extension and compression of Mn-O bond pairs and is directly correlated with Jahn-Teller distortion, provides a strong basis for the changes that occur at the level of MnO_6 octahedra which provides the physical basis for the change in the optical properties of the NPs upon functionalization. Moreover, the direct bonding of tartrate ligands to the surface of the LSMO NP has been confirmed by FTIR spectroscopy (Fig. 24b). As shown in Fig. 24c, transmission electron microscopy (TEM) revealed that T-LSMO NPs are nearly spherical in shape with an average diameter of around 4 nm (Fig. 24d). The HRTEM image (Fig. 24e) confirm the crystalline nature of the T-LSMO NPs having interplanar distance of 0.267 nm, which corresponds to the (110) plane of the crystal lattice.

3.2.3. Understanding the key photophysical processes at the nano-bio interface between Mn_3O_4 NPs and organic biomolecules^[49]

Surface modification can have a significant influence on the materials behavior at the nanoscale and can lead to nanostructures with novel properties. Here, we demonstrate surface modification induced multiple photoluminescence and room temperature ferromagnetic activation of Mn_3O_4 NPs.

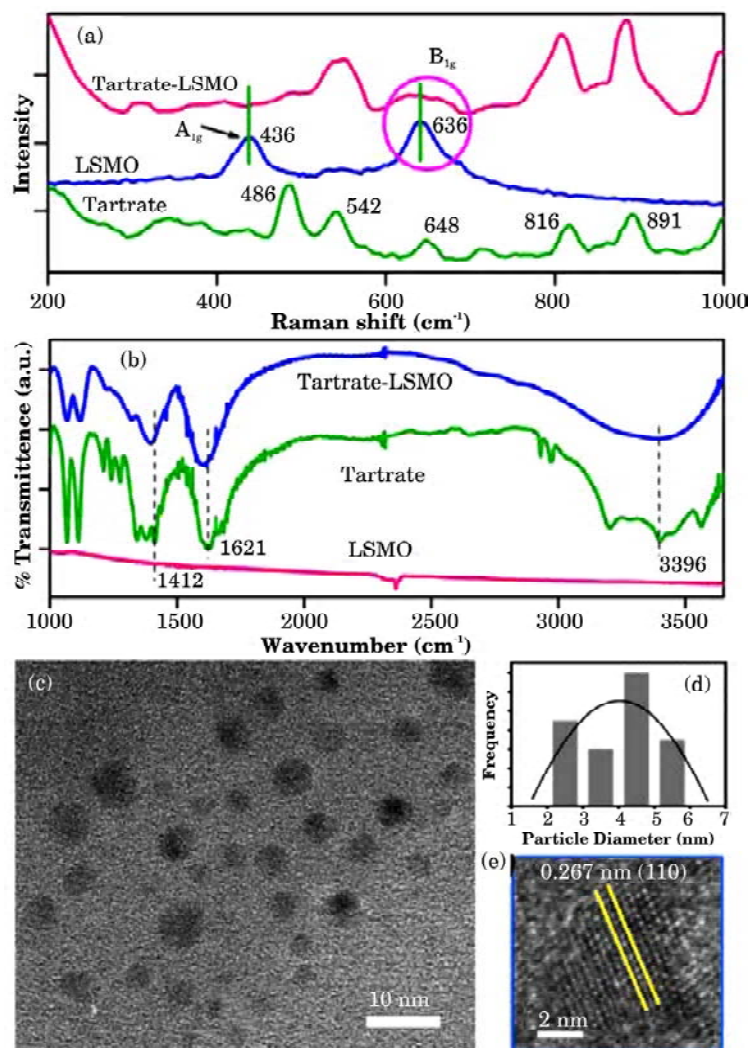


Fig. 24: a) Raman spectra of as-prepared LSMO NPs, tartrate-LSMO NPs and tartrate. b) FTIR spectra of as prepared LSMO NPs, sodium tartrate and tartrate functionalized LSMO (tartrate-LSMO) NPs, recorded with a KBr pellet. c) TEM image of tartrate-LSMO NPs. d) Size distribution of the NPs in solution. e) HRTEM image of the crystalline structure of tartrate-LSMO NPs.

Employing a systematic variation of the ligands, their functional groups and the structural position of the functional groups, we have identified the necessary and sufficient structural requirement of the surface co-ordinating ligands, to induce such unprecedented optical/magnetic responses from the NPs. Using a multitude of spectroscopic techniques, we have investigated the mechanistic insight behind this emergence of multiple PL and it is revealed that, the presence of a α -hydroxy carboxylate moiety in the ligands is necessary to activate the Jahn–Teller (J–T) splitting of Mn^{3+} ions on the NPs surface and the corresponding d – d transitions along with ligand–to–metal charge transfer transitions (LMCT, associated with $\text{Mn}^{2+/3+}$ –ligand interactions) plays the deciding role. Whereas, the presence of a carboxylate group in the surface coordinating ligands is sufficient to activate the room temperature ferromagnetism of the NPs. Moreover, it has been observed that the ligands induce smallest crystal field splitting energy (CFSE) resulted in the strongest ferromagnetic activation of the NPs. Finally, the functionalized material has been identified as an efficient catalyst for the photo–degradation of a model cationic organic dye. Apart from the fundamental scientific interest, these results represent a promising route for the rational designing of Mn_3O_4 NPs adaptable to diverse applications.

Synthesis of Mn_3O_4 NPs

We have synthesized the bulk Mn_3O_4 nanoparticles following a reported procedure where an ultrasonic–assisted approach has been used to prepare colloidal Mn_3O_4 nanoparticles at normal temperature and pressure without any additional surfactant or template^[50].

Functionalization of as–prepared Mn_3O_4 NPs by different ligands to prepare ligand functionalized– Mn_3O_4 NPs

In all cases, first we have prepared 0.5 M ligands solution in Milli–Q (from Millipore) water. Then we have adjusted the pH of the solutions at ~7 by addition of 1 (M) sodium hydroxide (NaOH) solution. In the ligand solution of pH~7, we have added as–prepared Mn_3O_4 NPs (approximately 100 mg powder Mn_3O_4 NPs in 5 mL ligand solution) and followed by extensive mixing for 12 hours in a cyclo–mixer. Finally, the non–functionalized bigger sized NPs were filtered out (by a syringe filter of 0.22 mm diameter) and the resulting filtrated solutions were used for our experiments. Functionalization of Mn_3O_4 NPs with small organic ligands causes significant changes to their surface electronic structures. Before intentional variation of the ligands, we have examined the UV–vis electronic absorption pattern of the as–prepared Mn_3O_4 NPs alone.

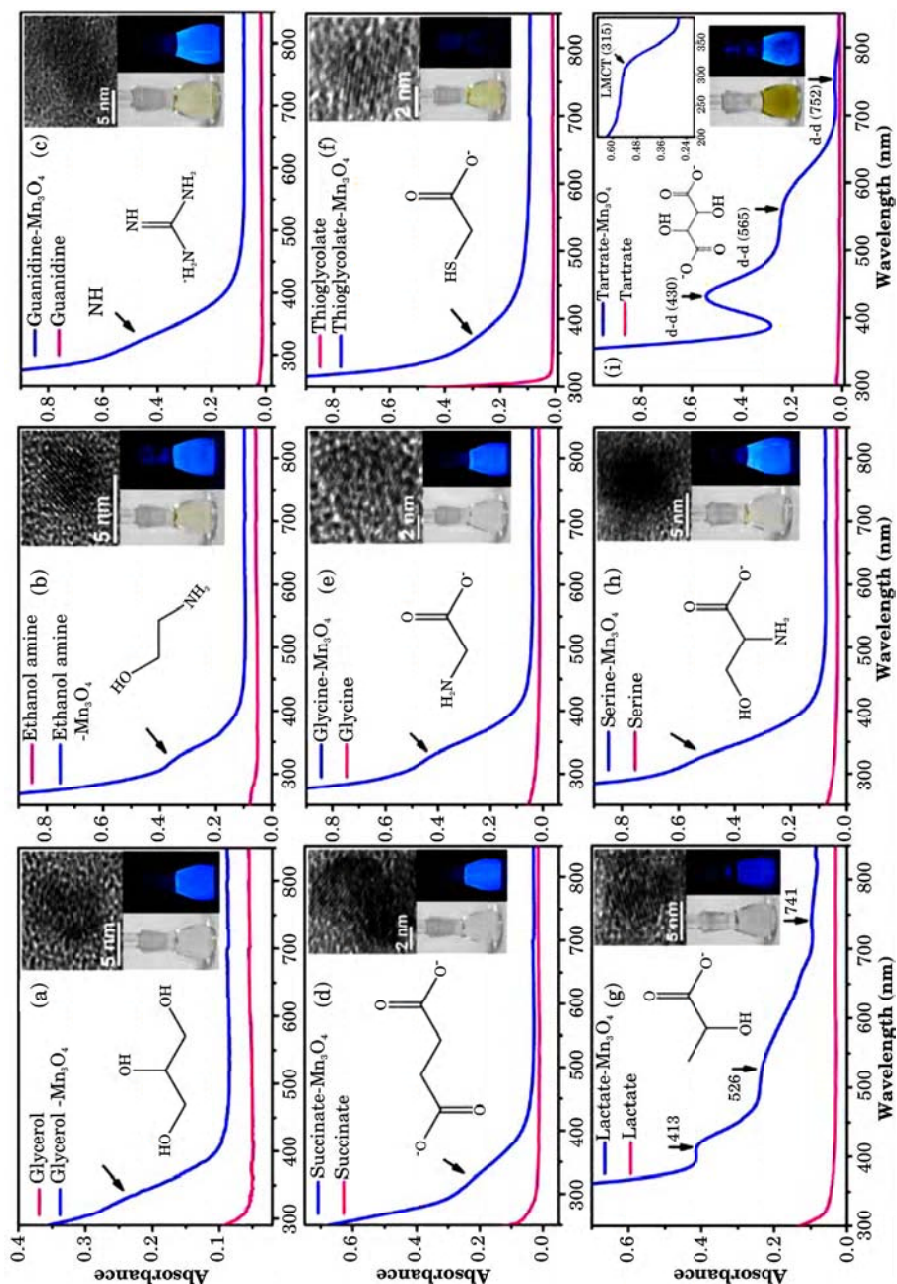


Fig. 25: a–i represents the UV–vis absorption spectra of ligand functionalized– Mn_3O_4 NPs in aqueous solution at pH~7. Different combinations of ligand functional groups have been employed in order to activate the Jahn–Teller (J–T) splitting of Mn^{3+} ions in the NPs surface and to bring out optimal optical responses from the functionalized NPs. (a) –OH (hydroxyl) group of glycerol (b) –OH and – NH_2 (hydroxyl and amine) groups of ethanol amine, (c) – NH_2 group of

Fig. 25: (Contd...)

guanidine, (d) -COO^- (carboxylate) group of succinate, (e) -COO^- and -NH_2 groups of glycine, (f) -COO^- and -SH (carboxylate and thiol) groups of thioglycolate, (g) -COO^- and -OH (at α position) groups of lactate, (h) -COO^- and -OH (at β position) groups of serine and (i) -COO^- and -OH (two α hydroxyl groups) groups of tartrate have been used respectively, to functionalize the as-prepared Mn_3O_4 NPs. Upper inset of Fig. a–h show the corresponding HRTEM image of various ligand functionalized Mn_3O_4 NPs. Photographs under visible (left) and UV light (right) of various ligand functionalized Mn_3O_4 NPs have been shown in the lower inset.

However, it has no such characteristic absorption signature in the UV–vis region. The absorption spectra recorded in Fig. 25 for ligand functionalized Mn_3O_4 NPs exhibit distinct features depending upon the types of ligand functional groups used. Fig. 25 a–f represent the absorption spectra of functionalized Mn_3O_4 NPs where -OH (hydroxyl group of glycerol), -OH and -NH_2 (hydroxyl and amine groups of ethanol amine), -NH_2 (amine group of guanidine), -COO^- (carboxylate group of succinate), -COO^- and -NH_2 (carboxylate and amine groups of glycine), and -COO^- and -SH (carboxylate and thiol groups of thioglycolate) functional groups of the ligands have been chosen to functionalize the NPs. In all cases, a characteristic absorption band (marked by arrows) between 300 and 360 nm has been observed. We assume that this high energy absorption band is the result of the interaction between the ligand functional group and the $\text{Mn}^{2+}/\text{Mn}^{3+}$ onto the NPs surface, therefore assigned as LMCT band. However, inclusion of a -OH group at the α position with respect to -COO^- *i.e.* in case of lactate– Mn_3O_4 (Fig 25g), the UV–vis absorption spectrum results distinctly different features at the low energy region. Even more interestingly, on shifting the structural position of the -OH group from α to β with respect to -COO^- *i.e.* in case of serine– Mn_3O_4 (although serine contains a α NH_2 group, however, results of glycine– Mn_3O_4 could be considered as control study), those low energy UV–vis bands vanishes. The observation clearly indicates that the origin of distinct absorption features is a special case only for α –hydroxy carboxylate (like lactate) moiety containing ligand functionalized Mn_3O_4 NPs. To further corroborate this phenomenon, we have employed tartrate ligands, having two α –hydroxy carboxylate groups, as a capping ligand. Akin to lactate– Mn_3O_4 , T– Mn_3O_4 possesses LMCT band as well as distinct even more pronounced absorption features at the low energy region. Thus, from the above investigation we can infer that the presence of α –hydroxy carboxylate moiety in the surface coordinating ligand is necessary to activate the observed distinct absorption features (detail identification of the absorption bands is discussed later in the text). Upper insets of Fig. 25a–h represent high resolution transmission electron microscopic (HRTEM) images of the

corresponding ligand functionalized Mn_3O_4 NPs showing their tentative diameters within 3–5 nm. Lower insets of Fig. 25a–i represent the photographs of various ligands functionalized Mn_3O_4 NPs under visible (left) and under UV light (right), respectively. Considering the optical responses obtained from T- Mn_3O_4 NPs as optimal, we have investigated only T- Mn_3O_4 NPs in detail in order to gain insights of the origin of these distinct absorption characteristics, bright PL under UV light and also the effect of further surface modification.

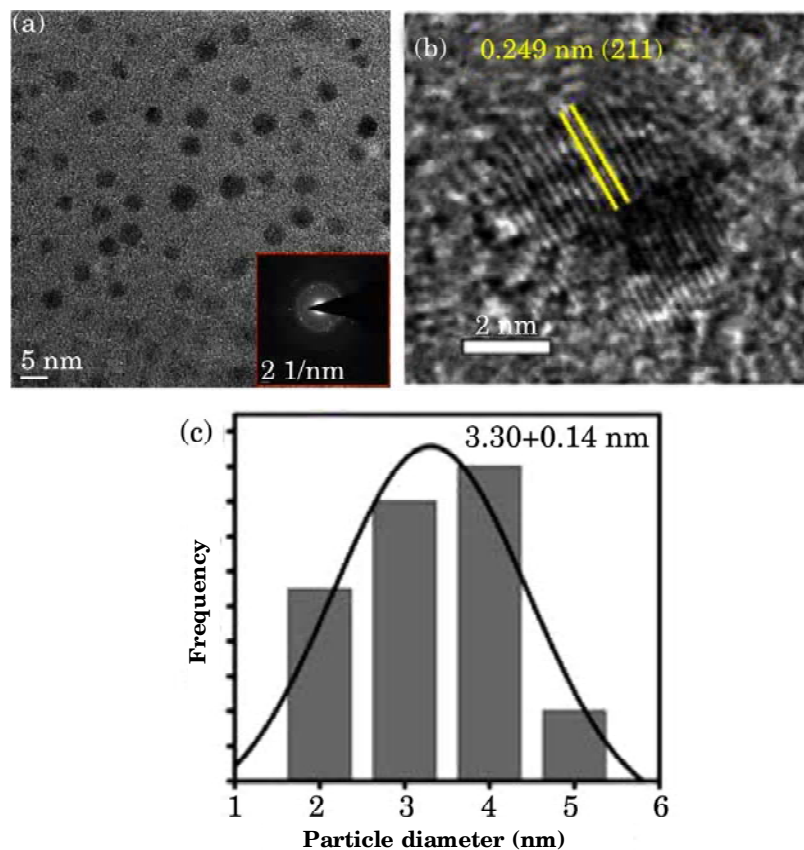


Fig. 26: (a) TEM image of T- Mn_3O_4 NPs. Inset shows the selective area electron diffraction (SAED) pattern of the T- Mn_3O_4 NPs. (b) HRTEM image of the crystalline structure of T- Mn_3O_4 NPs. (c) Size distribution of the T- Mn_3O_4 NPs.

TEM study has been carried out in order to characterize the water soluble T- Mn_3O_4 NPs in details and also to substantiate the functionalization process. As shown in Fig. 26a, T- Mn_3O_4 NPs have a broad size distribution (1.5–5.5 nm) with an average diameter of $3.30 \pm$

0.14 nm (Fig. 26c) and nearly spherical in shape. The corresponding HRTEM image (Fig 26b) confirms the crystallinity of the NPs. The interplanar distance between the fringes is about 0.249 nm which corresponds to the distance between (211) planes of Mn_3O_4 tetragonal crystal lattice.

Photophysical processes at the interface between Mn_3O_4 NPs and tartrate ligands

In Fig. 25i, the UV-vis absorption spectra of T- Mn_3O_4 NPs (at pH ~ 7) exhibits two absorption peaks at 315 (shown in the inset) and 430 nm, a shoulder descending into lower energies around 565 nm and a broad band at 752 nm. The observed peak at 315 nm could be assigned to the possible high energy LMCT processes involving tartrate- $\text{Mn}^{2+}/\text{Mn}^{3+}$ interactions^[43]. Other bands at 430, 565 and 752 nm are attributed to d-d transitions of Mn^{3+} in T- Mn_3O_4 NPs, as the degeneracy of $5E_g$ ground state term of d^4 (Mn^{3+}) in high-spin octahedral environment has been lifted by the J-T effect, that leads to the observed bands for the transitions of $5B_{1g} \rightarrow 5E_g$, $5B_{1g} \rightarrow 5B_{2g}$ and $5B_{1g} \rightarrow 5A_{1g}$, respectively^[44,51]. In case of as-prepared T- Mn_3O_4 NPs (at pH~7), LMCT excited state has been observed to be strongly photoluminescent, whereas, PL from d-d excited states have been found considerably week. Thus, in order to make d-d excited states highly photoluminescent, we have heat-treated as prepared T- Mn_3O_4 NPs at pH ~12 and 70°C for 12 hrs. As evident from Fig. 27a, the UV-vis absorption spectrum of heat treated T- Mn_3O_4 NPs changes from the initial spectrum of T- Mn_3O_4 NPs (Fig. 25i). Specifically, the peak at 430 nm and lower energy shoulder at 565 nm (both originate due to d-d transitions involving Mn^{3+}) are significantly perturbed and blue shifted to 385 and 440 nm, respectively. However, the LMCT band at 315 nm and another d-d band at 758 nm remain almost unaffected. Inset of Fig. 27a shows the fluorescence microscopic images of powder containing T- Mn_3O_4 NPs (after treatment) under irradiation of white light (bright field, I) and light of two different wavelengths (II-365 nm and III-436 nm), respectively. Multi-colored PL arising from different excitation of the NPs are clearly evident from the photographs. Fig. 27b shows the normalized PL spectra of T- Mn_3O_4 NPs at room temperature and pH ~12. Multiple PL of T- Mn_3O_4 NPs starting from blue, cyan, green to near-infrared region (PL maximum at 417, 473, 515 and 834 nm) of the spectra against excitation at four different wavelengths (315, 370, 440 and 760 nm, respectively) are clearly evident from the figure. In the excitation spectra (Fig. 27c) of T- Mn_3O_4 NPs at their respective PL maxima, the observed peaks/bands have a direct correlation with the absorption peaks/bands involving LMCT and d-d transitions (Fig. 27a).

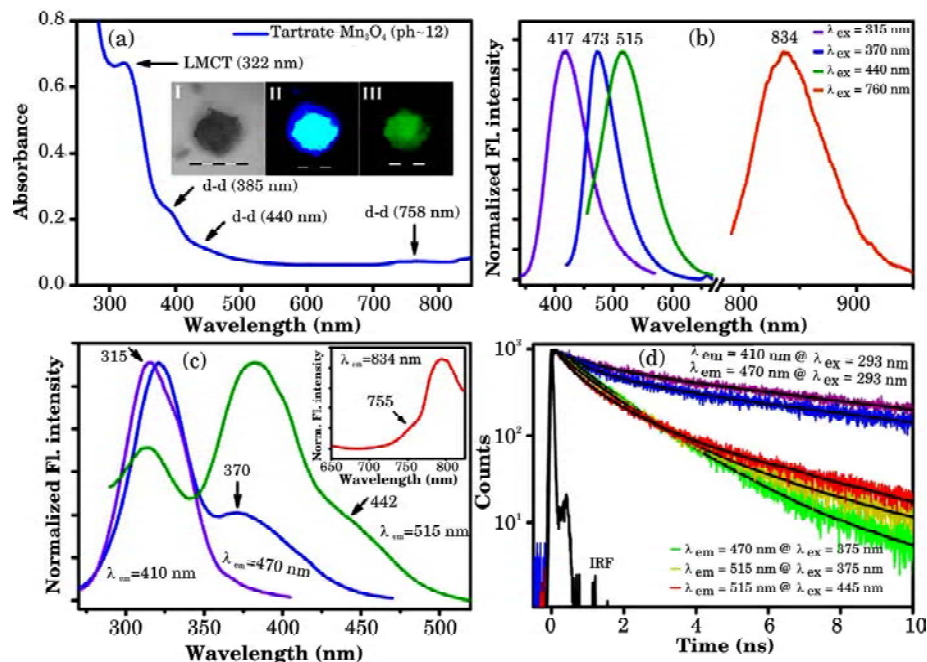


Fig. 27: a) UV-vis absorption spectrum of T-Mn₃O₄ NPs after treatment (at pH ~12 and 70°C for 12 hrs). Inset shows the fluorescence microscopic images of the same under irradiation of white light (bright field, I) and light of two different wavelengths 365 (II) and 436 (III) nm. Scale bars in the images are of 500 μ m. b) Normalized steady-state PL spectra collected from T-Mn₃O₄ NPs with four different excitation wavelengths of 315, 370, 440 and 760 nm at pH-12. c) Excitation spectra of T-Mn₃O₄ NPs at different PL maxima of 410, 470, 515 and 834 nm. d) Picosecond-resolved PL transients of T-Mn₃O₄ NPs in water measured at emission wavelengths of 410, 470 and 515 nm upon excitation with excitation source of 293, 375 and 445 nm wavelengths.

Thus, the PL as shown in Fig. 27b may be assigned to originate predominantly from the LMCT [tartrate \rightarrow Mn³⁺] excited states and ligand field excited states of the metal (Mn³⁺) d orbitals. PL from either an intraligand or metal to ligand charge-transfer (MLCT) excited states are considered unlikely. In case of other ligand functionalized Mn₃O₄ NPs having solely LMCT absorption band *e.g.* succinate-Mn₃O₄, single PL with a maximum around 410 nm has been observed.

Picosecond-resolved PL decay transients of T-Mn₃O₄ NPs have been collected to further understand the origin of PL due to the functionalization of the NPs. Fig. 27d represents the PL decay transients of T-Mn₃O₄ NPs at three different PL maxima of 410, 470 and 515 nm using three different excitation sources of 293, 375 and 445 nm wavelengths, respectively. The observed differences in the excited-state lifetime of T-Mn₃O₄ NPs at 410 nm PL compared to the lifetimes at 470

and 515 nm PL, suggest a difference in the origin of the PL. The average lifetime (τ) for 470 and 515 nm PL (upon excitation by 375 and 445 nm sources, respectively) have been observed to be 1.13 and 0.78 ns respectively, whereas, relatively longer τ of 5.32 ns has been observed for 410 nm PL (Table 2). Thus, the lifetime data and steady-state measurements clearly suggest that LMCT excited states are responsible for PL at 417 nm, whereas the J-T excited states lead to the PL maxima at 470, 515 and 834 nm.

Table 2: Lifetime values of picosecond time-resolved PL transients of T-Mn₃O₄ NPs, detected at various PL maxima upon excitation at different wavelengths. The Values in parentheses represent the relative weight percentage of the time components.

System	Excitation wavelength, λ_{ex} (nm)	Photoluminescence peak, λ_{em} (nm)	τ_1 (ns)	τ_2 (ns)	τ_3 (ns)	τ_{av} (ns)
T-Mn ₃	293	410	0.26 (11)	1.05 (29)	8.37 (60)	5.32
O ₄ NPs	293	470	0.54 (29)	1.43 (29)	8.20 (42)	4.04
	375	470	0.43 (20)	1.16 (74)	3.09 (6)	1.13
	375	515	0.18 (30)	1.06 (62)	3.93 (8)	1.03
	445	515	0.18 (47)	0.87 (44)	3.58 (9)	0.78

Effect of surface modification on the magnetic behaviour of Mn₃O₄ NPs

To study the effect of surface bound ligands on the magnetic behaviour of Mn₃O₄ NPs, we have characterized both as-prepared and ligand functionalized NPs, where the nature of the surface ligands was varied depending on their functional groups. Fig. 28 shows the applied field dependent magnetization measurements (M-H curves) at room temperature (300 K). M-H curve (inset of Fig. 28a) of as-prepared Mn₃O₄ NPs is linear with the applied field and has no hysteresis loop at 300 K, indicating the paramagnetic behaviour of the nanocrystals, which is as expected. However, at 300 K, the M-H curve of each ligand functionalized-Mn₃O₄ NPs represents a distinctly different response of magnetization compared to the as-prepared NPs. Clearly, each ligand evokes different magnitude of ferromagnetism to the as-prepared Mn₃O₄ NPs upon functionalization. While the room temperature ferromagnetism can be activated by functionalization with glycerol and guanidine, it can be further enhanced by succinate and tartrate (Fig. 28a-d). Both succinate and tartrate functionalized Mn₃O₄ NPs show well-defined hysteresis loop with saturation magnetization and coercive field (H_C) of around 2×10^{-3} emu/g and 105 Oe, respectively. According to ligand field theory, transition metal ions having a larger d orbital

splitting energy due to ligand coordination should have a smaller spin-orbit coupling^[52]. Any decrease in the spin-orbit coupling of surface magnetic cations results a smaller surface magnetic anisotropy and subsequently the coercivity of the NPs will be reduced^[53]. It is also well known that σ donor ligands result in larger CFSE than π donors^[52]. Among the four ligands used for magnetic measurements, glycerol (having $-\text{OH}$ group) and guanidine ($-\text{NH}_2$) are in the class of σ donor, tartrate having both σ donor ($-\text{OH}$) and π donor ($-\text{COO}^-$) properties, whereas, succinate (having only $-\text{COO}^-$) is a π donor ligand^[52]. Thus, because of the higher CFSE, glycerol and guanidine functionalized Mn_3O_4 NPs show no coercivity, however, tartrate and succinate functionalized NPs show coercivity of 97.5 and 109 Oe, respectively.

Photocatalytic activity of the surface modified $T\text{-Mn}_3\text{O}_4$ NPs

Uses of Mn_3O_4 nanocrystals having different morphologies as a catalyst for the degradation of cationic organic dye have been reported recently; however, in all cases the degradation rate is very slow^[54,55].

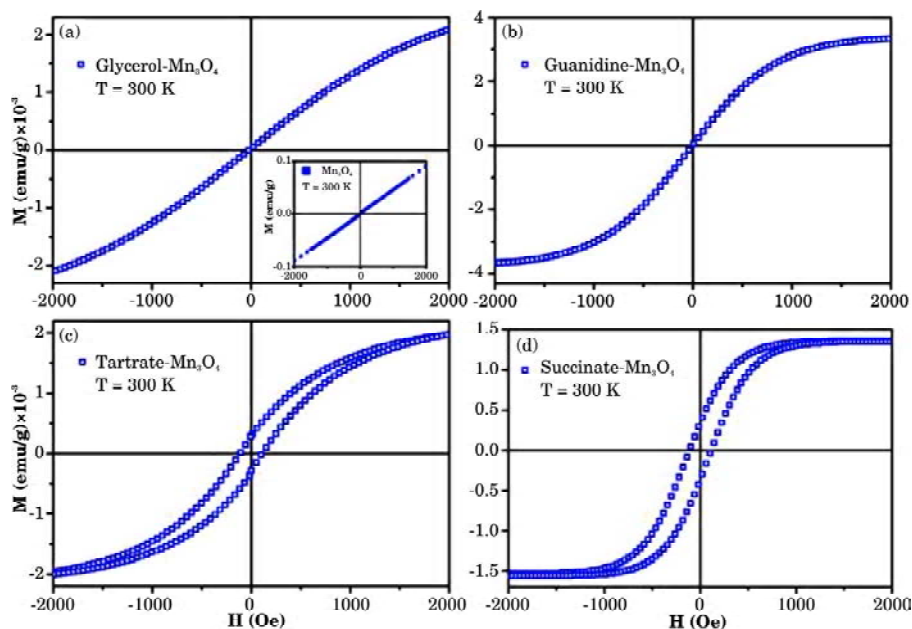


Fig. 28: Field dependent magnetization (M vs H) at room temperature (300 K) (a) glycerol- Mn_3O_4 , (b) guanidine- Mn_3O_4 , (c) tartrate- Mn_3O_4 and (d) succinate- Mn_3O_4 NPs. Inset shows the same for as-prepared Mn_3O_4 NPs. The distinct hysteresis loop observed in case of c and d confirm ferromagnetic activation of the NPs upon functionalization with carboxylate ligand.

We have observed that our surface modified T-Mn₃O₄ NPs have better photocatalytic activity towards a model cationic organic dye (methylene blue) compared to other existing reports, thus, we infer that the increased surface reactivity and PL of T-Mn₃O₄ NPs plays an important role in enhancing the catalytic activity (Fig. 29).

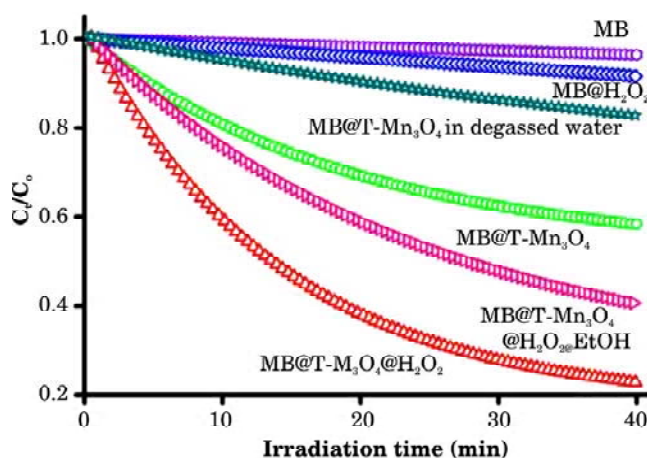


Fig. 29: Plots of relative concentration (C_t/C_0) versus time for the photodegradation of MB (monitored at 660 nm) alone and in presence of T-Mn₃O₄ NPs, H₂O₂, T-Mn₃O₄@H₂O₂ and T-Mn₃O₄@H₂O₂@EtOH, are shown.

3.3. Semiconductor-Based Nanobiomaterials

3.3.1. Protein-directed synthesis of *nir*-emitting, tunable HgS quantum dots and their applications in metal-ion sensing^[56]

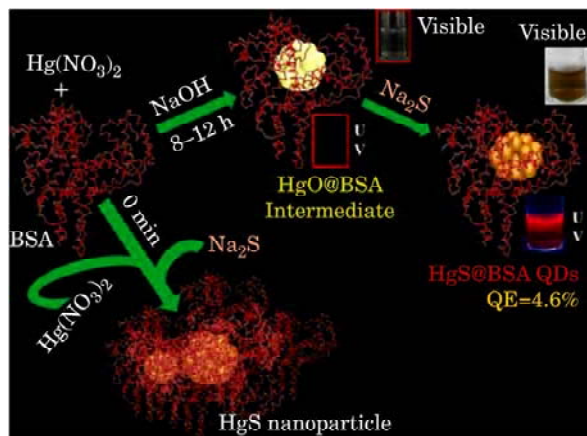
Among many biological systems that could participate in bio-mineralization and be incorporated into bio-nanomaterials, proteins have been the subject of particular attention due to their nanoscale dimensions, distinctive molecular structures and functionalities, and their capability to control the size of inorganic crystals during nucleation and growth to a remarkable degree due to their bulky nature. For example, bovine serum albumin (BSA) and several other proteins have been used to synthesize sub-nanometer sized luminescent metal clusters^[40,57-61]. Recently, aqueous, protein-driven synthesis of transition metal-doped ZnS QDs has also been reported by Zhou *et al.*^[62] Akin to the bio-mineralization process, herein, we have developed a facile approach to prepare water-soluble, highly stable NIR-luminescent HgS QDs, which are protected and stabilized by the protein matrix. We have also used the HgS QDs as fluorometric sensor for the detection of Hg(II) and Cu(II) ions. Uses of the QDs in metal ion sensing by exploiting their luminescence properties is not new and have been

reported before^[63,64]. The mechanisms of the luminescence quenching involving inner-filter effects, non-radiative recombination pathways and electron transfer processes have also been reported. However, the quenching mechanisms addressing the specific interaction of detected ions with the sensor QDs are sparse in the existing literature. The reason for quenching relies on the metallophilic interaction between Hg(II)/Cu(II) and Hg(II) present on the surface of the HgS QDs. We have used time-resolved luminescence methods to study the mechanism of excited-state reactivity which reveals that both Hg(II) and Cu(II) ion can reduce the lifetime of the HgS QDs. After considering all kind of excited state deactivation mechanisms, we have found that Dexter energy transfer is the reason in case of Hg(II) ion induced quenching whereas photoinduced electron transfer dominates in case of Cu(II) ion induced quenching. In several control experiments, we have also ruled out other possibilities of the quenching mechanisms including aggregation, FRET etc.

Synthesis and characterization of HgS-Protein bio-nanoconjugates

The process for synthesizing the HgS QDs is simple and involves two steps (see experimental section for details). The various stages of synthesis are shown in Scheme 2. In the first step, addition of mercury nitrate solution to aqueous BSA causes the mercury ions to be coordinated with the various functional groups of BSA such as -SH, -NH, etc. The pH of the solution was adjusted to ~9 by the addition of NaOH followed by vigorous stirring at room temperature. After 8–12 hrs the colour of the solution changes from colourless to pale yellow intermediate which we have analyzed by Raman spectroscopy and found it to be HgO@BSA. Photographs of the intermediate under UV and visible light are shown in Scheme 2. In the last step, Na₂S is added and the color changes from pale yellow to light brown (Scheme 2) which indicates the formation of HgS QDs.

Figure 30a illustrates the UV-vis absorption spectra of HgS@BSA QDs. In particular, Fig. 30a gives the plot of the natural logarithm of the Jacobian factor versus wavelength of the QDs, to show the features more clearly. Well-defined absorption features are marked with arrows. Three distinct excitonic absorption shoulders of the HgS QDs are found at 473 (2.62), 546 (2.27) and 594 nm (2.09 eV), respectively which indicate the presence of different size QDs. The band gaps calculated for UV features at 2.62, 2.27, and 2.09 eV are 2.02, 1.94 and 1.90 eV, respectively, which are very much blue shifted from the average band gap of bulk β -HgS (-0.2 to 0.5 eV)^[65] due to high quantum confinement effect. Fig. 30b shows the luminescence profile of the as-prepared QDs. A clear excitation maximum at 550 nm and luminescence peak at around 730



Scheme 2: Schematic illustration of the synthesis of HgS QDs through the bio-mineralization process mediated by BSA protein.

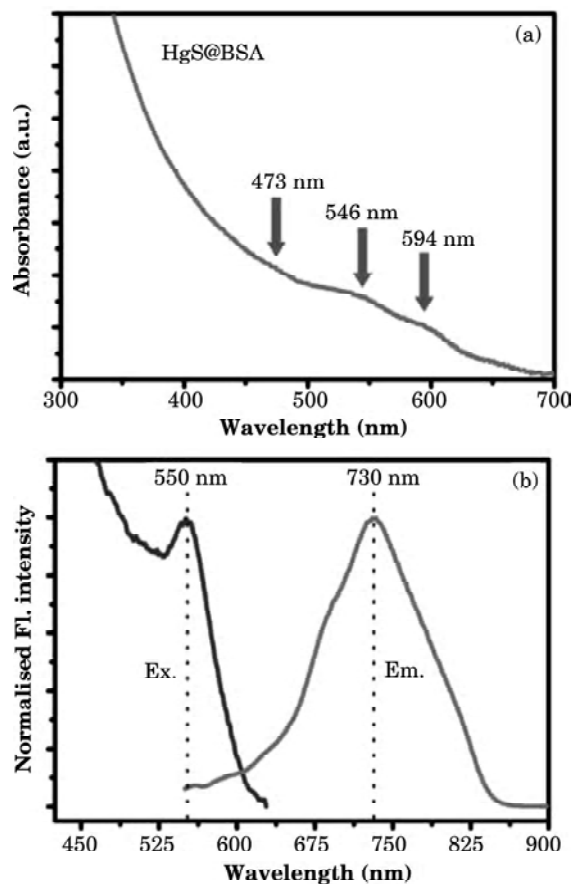


Fig. 30: (a) UV vis absorbance spectrum of HgS@BSA. (b) Excitation and emission spectrum of HgS@BSA. Excitation spectrum is taken by monitoring at 730 nm. Luminescence spectrum is collected with 450 nm excitation.

nm is evident from Fig. 30B. Note that, similar to the absorption spectrum, the luminescence spectrum is also broad and can be fitted into three different peaks having maxima at 680 (1.82), 733 (1.69) and 803 nm (1.54 eV). Photographs of QDs under UV and visible radiations are shown in Scheme 2.

By varying the experimental conditions, *e.g.*, Hg/S ratio we have achieved the variation of QDs diameter, resulting the tunability of their luminescence (Fig. 31a). As shown in Fig. 31b, a variation of excitation peak maxima is clearly observed, pointing to the presence of QDs having different sizes. In photoluminescence spectra the peak maxima varied from 680–800 nm which corresponds to a QD diameter from 4–10 nm according to our DLS results (Fig. 31c).

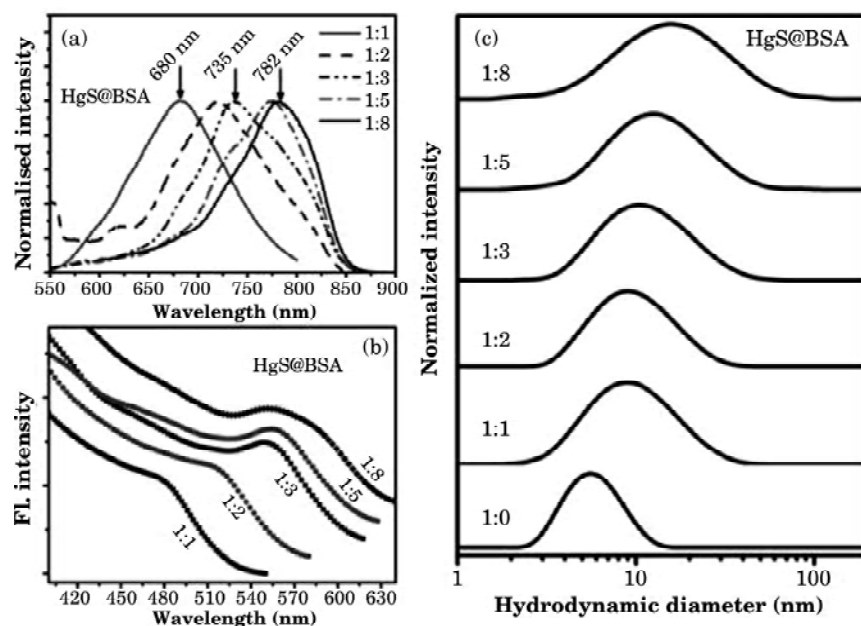


Fig. 31: Normalized spectra. (a) Luminescence, (b) excitation and (c) dynamic light scattering spectra for HgS@BSA QDs with different Hg/S molar ratio.

A high-resolution transmission electron microscopy (HR-TEM) image confirmed the presence of nearly spherical nanocrystals having a size of 3.8 ± 0.2 nm (Fig. 32a). As shown in Fig. 32b, characteristic hydrodynamic diameter of BSA is shifted from $5.6 (\pm 0.6)$ nm to $9.3 (\pm 0.6)$ nm in DLS after the formation of HgS QDs. This observation is consistent with the fact that QDs are formed within the protein matrix. Again, the size obtained from the TEM study is roughly comparable to the swelling of the protein size ($\sim 4.4 \pm 0.6$ nm), as revealed from our DLS

measurements. HR-TEM image of the HgS QDs is shown in Fig. 32c. The distance between two adjacent planes is 0.29 nm, corresponding to the (200) lattice plane of cubic β -HgS. Fig. 32D demonstrates the EDAX spectrum of the HgS@BSA. SEM image of the HgS@BSA and EDAX maps using C K, O K, S K, Hg L and Na K are shown in the inset of Fig. 32d.

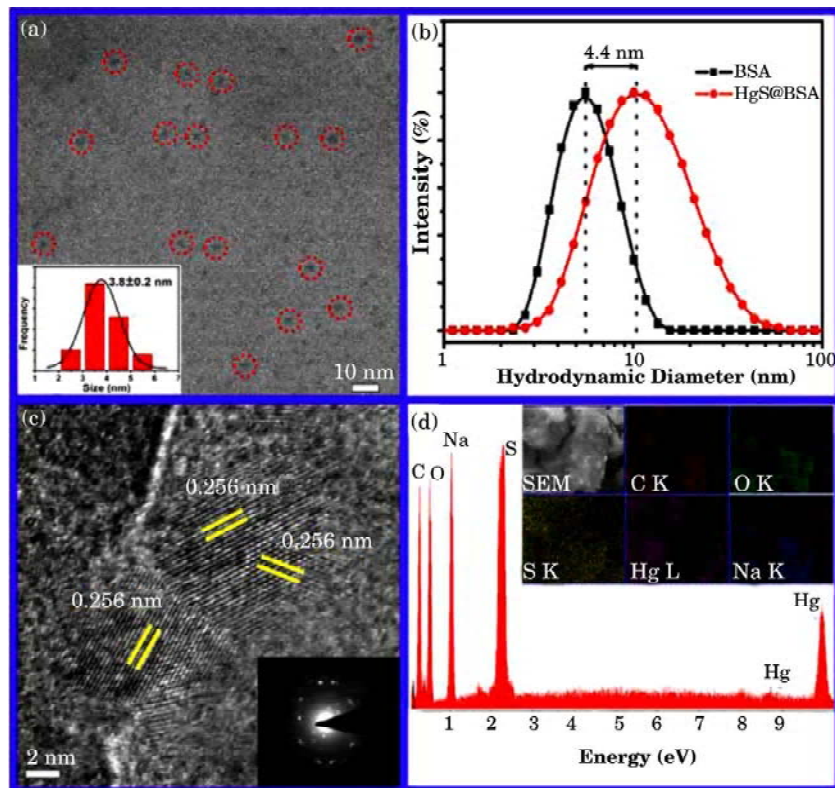


Fig. 32: (a) Typical TEM images of HgS QDs. The size distribution of HgS@BSA is shown in the inset. (b) Dynamic light scattering spectra of BSA (black) and HgS@BSA in aqueous solution at pH-9. The swelling of the protein size by 4.4 nm has also been assigned. (c) High-resolution TEM micrograph of HgS QDs. SAED pattern in an area including HgS QDs is shown in the inset. (d) EDAX spectrum collected from HgS@BSA. Inset showing the SEM image of the HgS@BSA sample from which the EDAX spectrum was taken. EDAX maps using C K, O K, S K, Hg L and Na K are also shown in the inset.

Metal ion sensing application of HgS@BSA bio-nanoconjugates

The optical responses of HgS QDs towards metal ions such as Hg(II), Ca(II), Cu(II), Co(II), Zn(II), Ni(II), Cd(II), Mg(II), Na(I), and K(I) have been investigated. Among these ions, only Cu(II) and Hg(II) can quench

the luminescence of the as-prepared HgS QDs. Fig. 33 demonstrates the high optical selectivity and sensitivity towards Cu(II) and Hg(II) over the other biologically relevant metal ions and could be seen with naked eye (Fig 33, lower panel). The mechanism to be proposed below is due to the following reasons: A number of sulphur and Hg(II) (having $5d^{10}6s^0$ electronic configuration) are present on the surface of the HgS QDs. Addition of metal ion to the HgS QD solution therefore generates two possibilities: either it will interact with sulphur or mercury. Moreover, sulphur has an affinity towards other metal ions including Hg(II), Cu(II), Zn(II) and Cd(II). Thus, if quenching of the luminescence of QDs occurs through the interaction with sulphur, then the all the above mentioned metal ions are expected to reduce the luminescence of HgS@BSA. However, almost insignificant change in the QDs luminescence spectrum with Zn(II) and Cd(II) as revealed from Fig. 33, clearly rules out the possibility of luminescence quenching through the interaction with sulphur. Recent theoretical studies suggest that metal centres with a d^{10} electronic configuration have a strong affinity towards other closed shell metal ions with similar electronic configuration^[66]. In particular, this phenomenon associated with strong $d^{10}-d^{10}$ interaction is known as metallophilic interaction^[67]. This interaction originates due to dispersive forces which are further augmented by relativistic effects^[67]. In the case of mercury ion ($5d^{10}6s^0$), a number of examples of such interactions are present in the literature, even in absence of protecting ligands^[57,58,68]. Our study suggests that luminescence quenching of HgS QDs in presence of Hg(II) is due to the same $5d^{10}-5d^{10}$ metallophilic interaction. In case of Cu(II), luminescence quenching could occur through $5d^{10}-3d^{10}$ metallophilic interaction as in the protein environment Cu(II) is reduced to Cu(I)^[69] (See Ref.^[56] for details mechanistic insight behind the metal ion sensing).

3.3.2. Direct conjugation of CdS nanocrystals to a globular protein^[70]

In the present study, we have used a mild reducing agent TCEP (tris (2-carboxyethyl) phosphine hydrochloride) to reduce specifically the solvent exposed disulfide bonds of a transporter protein human serum albumin (HSA) at pH 4.5. Semiconductor nanocrystal CdS has been grown amid the reduced disulfide linkage of the protein. The whole reaction has been carried out under an inert argon environment.

Moderate retardation of the enzymatic activity and insignificant perturbation of structural integrity of the enzyme upon attachment of the CdS nanocrystals reveal the merit of the covalent synthesis to probe the functionality of a protein in a physiological environment. Here, the

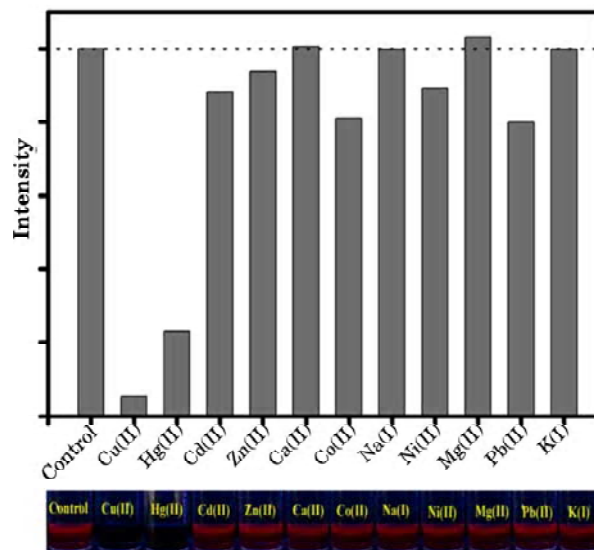


Fig. 33: Upper panel. Selectivity of the HgS@BSA to different metal ions. The luminescence intensities are recorded at 730 nm. For all cases, the final metal ion concentrations are 50 ppm. Dotted line refers to see the change of luminescence with respect to the control one. Lower panel. Photographs of the HgS@BSA solution under UV light after addition of 50 ppm of various metal ions.

covalently bound CdS quantum dot has been employed for the first time as an optical Förster resonance energy transfer (FRET) probe for the detection of protein–folding intermediates.

Characterization of the synthesized CdS–HSA bio–nanoconjugates

The covalent binding of CdS to HSA is confirmed by matrix assisted laser desorption ionization (MALDI)–mass spectrometry analysis (Fig. 34a). A peak at 66809.86 Da corresponding to the molecular mass of unlabeled HSA shifts to 67888.38 Da for the CdS–labeled HSA. The increase of the mass of HSA–CdS nanocomposites of 1078.52 Da is equivalent to 7.5 CdS (formula weight 144) molecules (15 atoms) in the nanocrystal conjugated to HSA. Theoretical estimation of the diameter of the CdS nanocrystals of 15 atoms reveals a value of ~1 nm on considering the crystal structure to be wurzite. The absorption spectrum of HSA–CdS exhibits a band ~370 nm (Fig. 34b), which indicates the presence of a quantized state of CdS nanoparticles. The blue–shifted absorption band with respect to the bulk CdS (~515 nm) is indicative of quantum confinement effect in the nanoparticles. The particle diameter and band gap are estimated to be 1.26 nm and 3.38 eV, respectively.

The observed photoluminescence band (Fig. 34b) centered at 528 nm is attributed to the recombination of charge carriers within surface states, which is also observed in the picosecond-resolved fluorescence transients (Fig. 34c). The quantum yield of HSA-CdS at 25°C is 0.49.

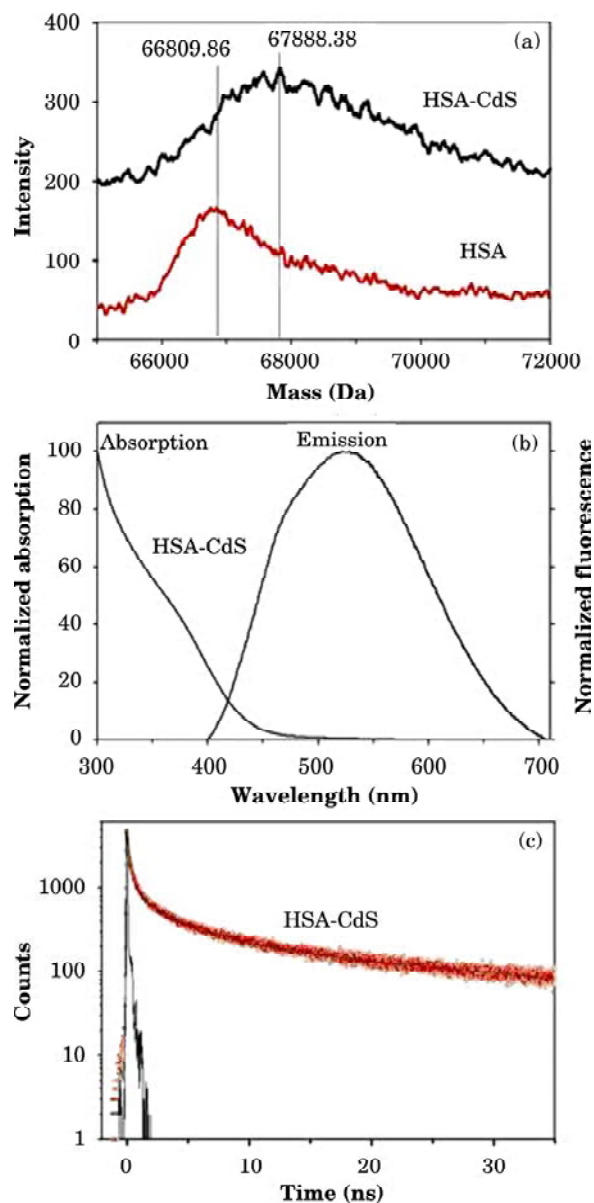


Fig. 34: (a) MALDI-mass spectrum of HSA and CdS labeled HSA (b) UV vis absorption and photoluminescence spectra of CdS in HSA-CdS (c) Picosecond-resolved photoluminescence transient of CdS in HSA (excitation wavelength 375 nm and detection wavelength 510 nm).

Resonance energy transfer from an intrinsic fluorescent amino acid Trp214 to the covalently attached CdS quantum dot

The efficiency of the intrinsic Trp214 in the globular transporter protein HSA as energy donor in FRET experiments has already been established in previous studies. Hence we concentrated on the dynamics of the FRET of Trp214 to a covalently attached cadmium sulfide (CdS) semiconductor QDs. The covalent binding of CdS to HSA is confirmed by Matrix assisted laser desorption ionization (MALDI)–mass spectrometry analysis. Fig. 35a shows the spectral overlap of the tryptophan emission (donor, emission maximum at 332 nm) and CdS excitation (acceptor, excitation spectrum maximum at 370 nm) in HSA at room temperature. The

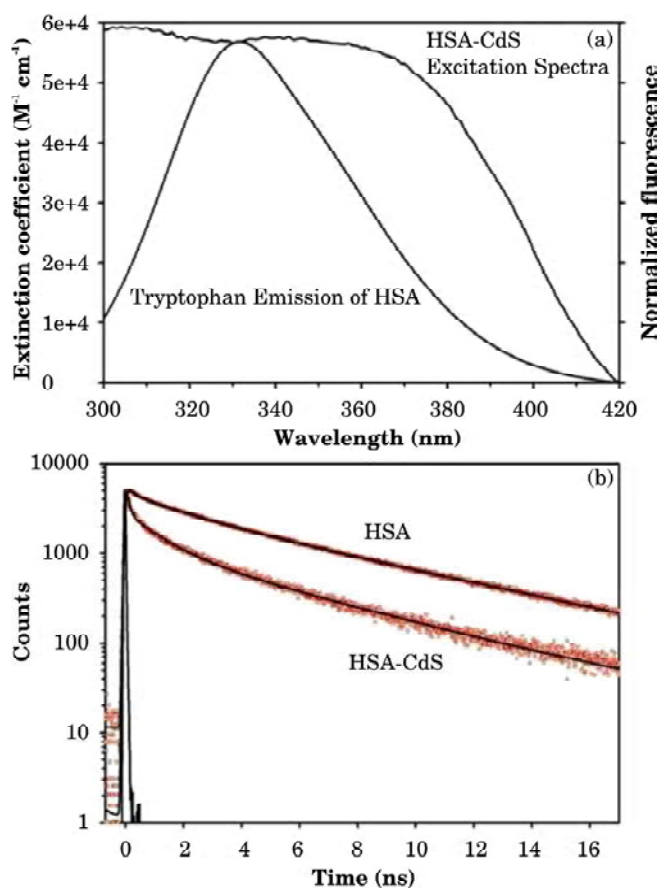


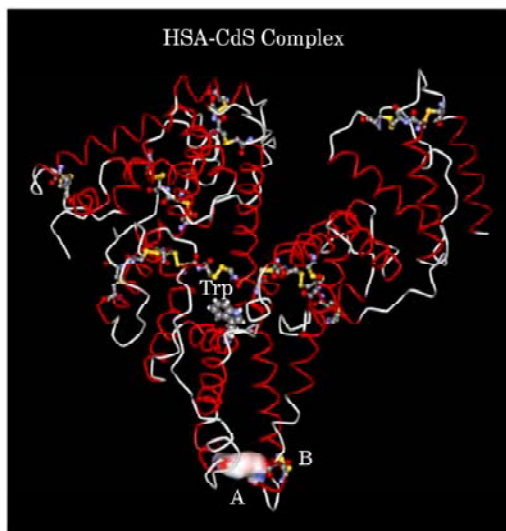
Fig. 35: (a) Spectral overlap between the donor (tryptophan in HSA, Trp214) emission and acceptor (CdS tagged with HSA) excitation (b) Picosecond–resolved fluorescence transients of Trp214 in HSA (excitation wavelength 299 nm and detection wavelength 360 nm) in absence and presence of CdS quantum dots in aqueous solution.

quenching of donor emission is evident from the faster lifetime (excitation source = 299 nm) associated with donor–acceptor pair (HSA labeled with CdS nanocrystal) compared to that in the donor alone (unlabeled HSA) (Fig. 35b).

The average D–A distance at room temperature is found to be 26.1 Å. The measured distance indicates that the possible locations of CdS are close to either Cys316–Cys361 (distance from Trp214 = 27.4 Å) or Cys360–Cys369 (distance from Trp214 = 27.5 Å) which are in subdomain IIB and significantly exposed to the solvent environment^[71], as indicated by A and B sites of (Scheme 3).

3.3.3. Multifunctional enzyme–capped ZnS bio–nanocomposites^[72]

The design of synthetic nanoparticles (NPs) capable of recognizing given chemical entities in a specific and predictable manner is of great fundamental and practical importance. Herein, we report a simple, fast, water soluble and green phosphine free colloidal synthesis route for the preparation of multifunctional enzyme–capped ZnS bio–nanocomposites (BNCs) with/without paramagnetic–ion doping.

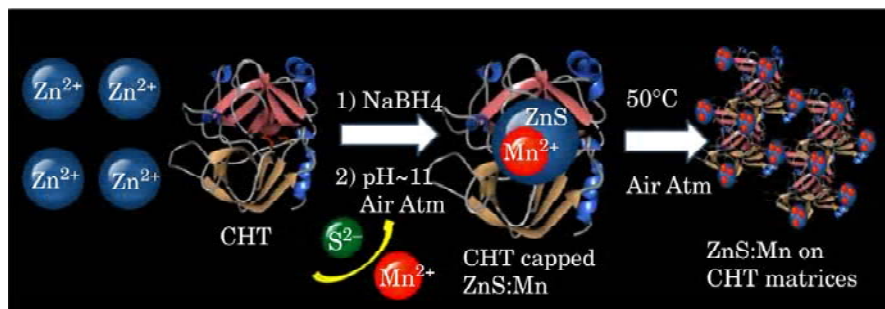


Scheme 3: Three dimensional structure of HSA is presented. The location of Tryptophan 214 (Trp) is indicated. The possible sites for CdS attachment, site A and site B essentially indicate the positions of the Cys316–Cys361 and Cys360–Cys369 disulfide bonds respectively. Nucleation of the nanocrystal is likely to occur in the site A (see text). The solvent accessible surface area (SASA) of site A is also shown. Ball–stick models are used to indicate other disulfide bonds of the protein. The coordinates of HSA structure is downloaded from protein data bank (PDB code 1UOR) and processed with WebLab Viewer Lite program.

The enzymes α -Chymotrypsin (CHT), associated with the NPs, are demonstrated as an effectual host for organic dye Methylene Blue (MB) revealing the molecular recognition of such dye molecules by the BNCs. An effective hosting of MB in the close proximity of ZnS NPs (with ~ 3 nm size) leads to photocatalysis of the dyes which has further been investigated with doped-semiconductors. The NP-associated enzyme α -CHT is found to be active towards a substrate (Ala-Ala-Phe-7-amido-4-methyl-coumarin), hence leads to significant enzyme catalysis. Irradiation induced luminescence enhancement (IILE) measurements on the BNCs clearly interpret the role of surface capping agents which protect against deep UV damaging of ZnS NPs.

Synthesis of CHT encapsulated ZnS bio-nanocomposites

The ZnS:Mn NPs were prepared by following general procedure modified from the reported literature^[73–78]. Briefly, 50 ml of 0.2 M L-Cys and 50 ml of 40 μ M CHT were taken into two different three-necked flasks and 200 μ M NaBH₄ was added in argon atmosphere with continuous stirring for 45 minutes. In the next step, 5 ml of 0.1 M [Zn(OAc)₂·2H₂O] were added into a three-necked flask. The mixed solution was adjusted to pH 11.0 with 2M NaOH and stirred under dry argon at room temperature for 30 min, and subsequently, 1.5 ml of 0.01 M [Mn(OAc)₂·4H₂O] was added into the above mixture and stirred for 20 min. 5 ml of 0.1 M deoxygenated Na₂S was injected into the solution quickly. The mixture was stirred for another 30 min, and then the solution was incubated at 50°C under air for 2 h in order to synthesize Cys and enzyme (CHT)-capped Mn-doped ZnS NPs. Finally, the colloidal NPs were dialysed against pure water for 4 h and 24 h for Cys-Zns:Mn and CHT-ZnS:Mn, respectively, at 4°C. The Cys-Zns and CHT-ZnS samples were prepared by using the above procedure except the addition of [Mn(OAc)₂·4H₂O]. The overall synthesis process is shown in Scheme 4.



Scheme 4: Synthetic strategy of enzyme mediated Mn-doped ZnS BNCs.

Characterization of the nano-biocomposite

Figure 36 shows a set of transmission electron microscopic (TEM) images of CHT and Cys-capped, with/without Mn²⁺ doped ZnS NPs which show well-separated NPs in the system. It has to be noted that the shape of the NPs in the protein matrix is relatively quasi-spherical compared to that of the Cys-capped NPs. The observation could be consistent with the fact that the NPs in the protein matrix are associated with a number of sulphur containing Cys residues from various locations of a protein which essentially direct the shape of the NPs to be quasi-spherical. On the other hand, plenty of free Cys residues in the solution for the Cys-capped NPs lead to uniform growth of the NPs and make the shape to be spherical. The corresponding high resolution TEM (HRTEM) images (right insets, Fig. 36a–d) clearly demonstrates lattice fringes with an observed d-spacing of ~0.31 nm and ~0.23 nm for CHT and Cys-capped NPs, which are in good agreement with the high-crystallinity in the materials with wurzite and zinc-blende structures, respectively^[79]. The particle size distributions (left insets, Fig. 36b, d) provide average diameter of 3 nm and 2.8 nm for the CHT and Cys-capped NPs, respectively. It is noticeable that CHT-capped NPs are fairly monodispersed in the protein matrix while for Cys-Zns:Mn, some of the particles are agglomerated up to 10 nm. Owing to the amino group capping on the surface, all the BNCs were steadily dispersed in water to form an optically transparent solution (Fig. 36e). Further confirmation of the composition and the crystal structure of as-prepared NPs are also evident from EDAX and SAED analysis. EDAX analysis (Fig. 36f) of the CHT-capped NPs reveals the incorporation of Mn with atomic contribution of 0.2% as dopant. A detailed analysis of SAED pattern (Fig. 36g) of CHT-capped NPs exhibits a cubic structure with distinct rings consistent with (311), (220), and (111) planes. On the other hand, analysis of SAED pattern (Fig. 36h) of Cys-capped NPs reveals a cubic structure with (311), (220), (111) and (102) distinguishable planes. The observation suggests that the crystal of Cys-ZnS:Mn NPs exist in the mixed form of cubic and hexagonal structure^[79].

We show the optical characterization of these BNC samples in terms of UV-visible absorption spectra and fluorescence spectra in Fig. 37. The UV-vis absorption spectra (Fig. 37a, b) show distinct absorption-edge at 320 nm for all the Cys and CHT-capped samples, respectively. Effective mass approximation⁸⁰ for the estimation of particle size from the shoulder of the absorption spectra of all samples at 320 nm reveals relatively larger particle size (5.3 nm) compared to that observed in the TEM image. The discrepancy could be due to the quasi-broad particle size distribution as evidenced in the TEM studies. It has also been shown

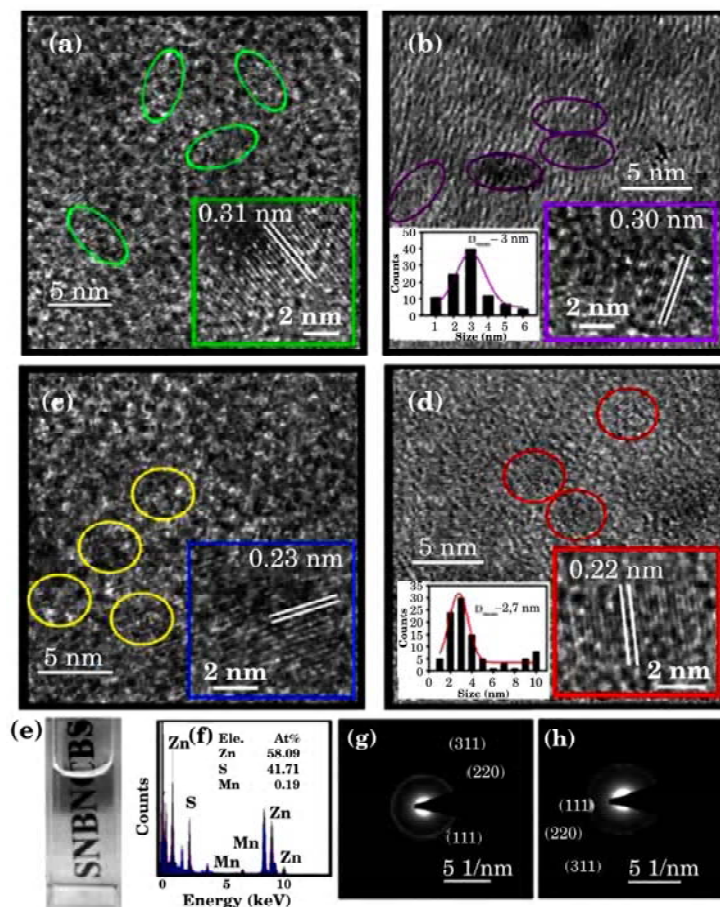


Fig. 36: Transmission electron microscopy (TEM) and high-resolution TEM images (inset) of (a) CHT-ZnS, (b) CHT-ZnS:Mn, (c) Cys-ZnS, (d) Cys-ZnS:Mn NPs. Inset left of Fig. (b) and (d) represent the size distribution analysis of CHT-ZnS NPs and Cys-ZnS:Mn NPs, respectively. Inset right of Fig. (b) and (d) represent the size distribution analysis of CHT-ZnS NPs and Cys-ZnS:Mn NPs, respectively. (e) Optically transparent solution of CHT-ZnS:Mn BNCs under daylight, (f) Energy-dispersive X-ray spectroscopy (EDAX) analysis and atomic percentages elements, (g) and (h) represent selected area electron diffraction (SAED) analysis of CHT-ZnS and CHT-ZnS:Mn BNCs, respectively.

earlier that UV-vis spectroscopy essentially reveals larger particles of samples containing multiple particle size distribution^[81,82].

The room temperature PL spectra (Fig. 37a, b) of doped and undoped ZnS NPs have been recorded at an excitation wavelength of 300 nm (4.13 eV). As shown in Fig. 37b, Cys-capped undoped ZnS NPs show one broad emission band centered at ~420 nm, which is attributed to defect-state recombinations, possibly at the surface. Since, an excess of

the cations have been used in the synthesis procedure, we expect sulphur vacancies at the surface giving rise to Zn dangling bonds that form shallow donor levels. Thus, the recombination is mainly between these shallow donor levels and the valence band. Becker *et al.* reported that S^{2-} vacancies even in bulk ZnS lead to emission at 428 nm^[83]. Upon Mn incorporation in nanocrystal samples, blue ZnS emission is quenched whereas an orange emission band develops at ~590 nm (Fig. 37b), corresponding to the spin forbidden ${}^4T_1-{}^6A_1$ Mn d-d transition in a tetrahedral site^[84-86]. The insets of Fig. 37a, b show PL photographs from the undoped (blue) and doped (orange) solutions upon 300 nm excitation. In the CHT-capped BNCs, NP associated proteins show a

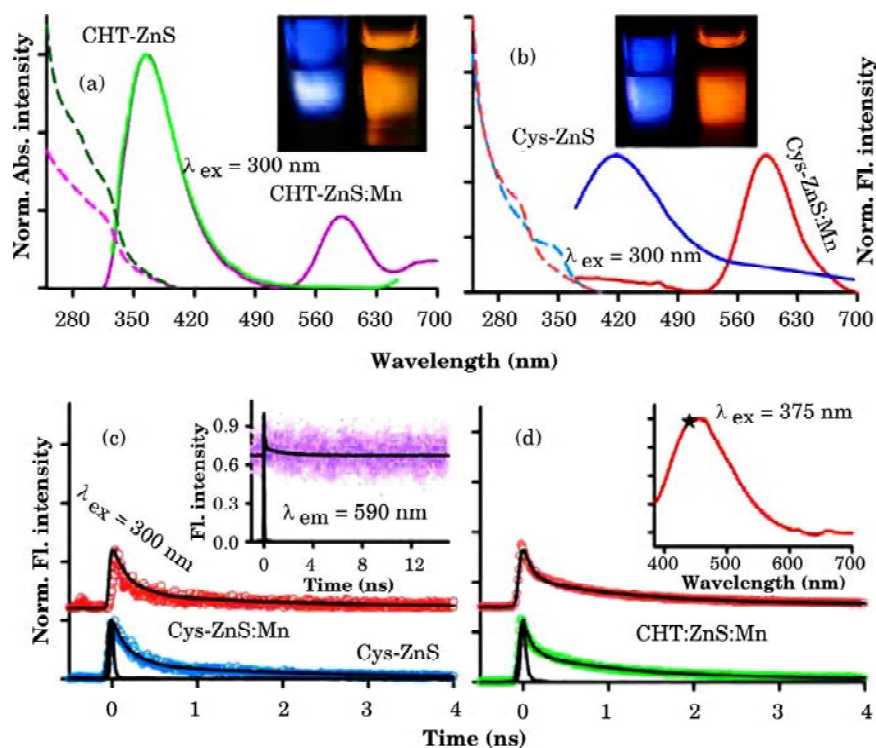


Fig. 37: (a) The optical absorption and steady-state emission spectra of (a) CHT-ZnS and CHT-ZnS:Mn BNCs and (b) Cys-ZnS, Cys-ZnS:Mn NPs, respectively. Inset of (a) and (b) shows PL photos of the corresponding solutions upon 300 nm excitation. (c) The picosecond-resolved fluorescence transients of Cys-ZnS and Cys-ZnS:Mn NPs (excitation at 300 nm) collected at 420 nm and inset shows fluorescence transient of Cys-ZnS:Mn NPs collected at 590 nm. (d) The picosecond-resolved fluorescence transients of CHT-ZnS:Mn NPs (excitation at 375 nm) collected at 460 nm (to avoid Raman scattering) and 590 nm. Inset shows PL spectra upon 375 nm excitation. A star sign represents the appearance of Raman scattering upon 375 nm excitation.

strong emission band centered at 367 nm (Fig. 37a), which possibly augments ZnS PL band at 420 nm^[87]. In the picosecond-resolved emission study (Fig. 37c), the excited state population of charge carriers in Cys-ZnS:Mn NPs are monitored at 420 nm followed by excitation at 300 nm. It is to be noted that Cys-ZnS and Cys-ZnS:Mn sample solutions show almost same decay pattern (time constants) when both the decays are monitored at 420 nm. This phenomenon reveals that the ZnS PL quenching upon Mn-doping is either static in nature or may be too fast to be resolved in our TCSPC instrument with IRF of 60 ps. Inset of Fig. 37c shows the time-resolved PL decay of Cys-ZnS:Mn NPs monitored at 590 nm. The PL transient is not completed in our experimental time window revealing higher values of time constants which are reported to be 1–2 ms in previous studies^[88,89]. Such a long lifetime makes the luminescence from the NPs readily distinguishable from the background luminescence from ZnS, which has a very short lifetime. On the other hand, in the cases of CHT-ZnS and CHT-ZnS:Mn BNCs, the strong emission from the protein essentially masks the ZnS emission and show characteristic decay of the intrinsic tryptophan residues of the protein in the picosecond-resolved transients at 420 nm. However, it is to be noted that CHT-ZnS:Mn samples show almost same decay pattern when detected at 590 nm and as a consequence, these advantages make them ideal candidates as fluorescence labelling agents, especially in biology^[82].

Upon below band-edge excitation (with 375 nm *i.e.* 3.3 eV), no Mn emission peak is noticeable in the doped NPs (Fig. 37d, inset). The picosecond-resolved fluorescence decays (excitation at 375 nm) monitored at 460 (to avoid Raman scattering at 428 nm) and 590 nm are shown in Fig. 37d which exhibits similar time constants of ZnS. The observation suggests that the below band-gap excitation is not sufficient to excite the doped material (Mn) via energy transfer from host's conduction band to Mn state^[82]. Considering that the excitation process generates an electron-hole pair across the band gap (3.9 eV) of the ZnS nanocrystal host, the present results make it obvious that there is a more efficient excitonic energy transfer from the host to the doped Mn site compared to that of the defect states in these materials; revealing a strong coupling between the Mn d levels and the host states^[90]. The energy transfer is unlikely to occur directly from the semiconductor trap (defect) states to the low-lying Mn d-states. This observation demonstrates that the trap states are not in a direct coupling with the Mn d-states and Mn-doping do not affect the trap state lifetimes of the excited state electrons at the host ZnS surface. Details of the spectroscopic parameters and the fitting parameters of the PL decays are tabulated in Table 3.

Table 3: Picosecond-resolved luminescence transients of Cys/CHT-capped ZnS NPs with/without Mn-doping^a.

<i>Samples</i>	<i>Excitation wavelength (nm)</i>	<i>Detection wavelength (nm)</i>	τ_1 (ns)	τ_2 (ns)	τ_{avg} (ns)
Cys-ZnS	300	420	0.20 (79%)	2.34 (21%)	0.65
Cys-ZnS:Mn	300	420	0.50 (88%)	3.49 (12%)	0.86
Cys-ZnS:Mn	300	590	4.5 (69%)	42.0 (31%)	16.1
CHT-ZnS:Mn	375	460	0.08 (92%)	2.89 (8%)	0.31
CHT-ZnS:Mn	375	590	0.13 (90%)	3.21 (10%)	0.44

^aThe emissions from ZnS NPs (probing at 420, 460 and 590 nm) were detected with a 300 and 375 nm laser excitation. Numbers in the parentheses indicate relative weightage.

Photocatalytic activity of the nano-biocomposite

To investigate the efficacy of the host protein matrix in promoting photogenerated charges from ZnS NP to a surface adsorbed molecule, we have performed photocatalysis of an organic dye methylene blue (MB, purchased from Carlo Erba). Bulk ZnS semiconductor with a large band gap (3.6 eV) produces electron-hole pairs under UV light that initiates the formation of surface radicals capable of oxidizing adsorbed organic and biological pollutants^[91,92]. In this work, photocatalytic activity was quantified by carrying out photoreduction of a test contaminant MB (Fig. 38a), which is known to be an excellent probe for the study of interfacial electron transfer in colloidal semiconductor systems^[93,94]. It is obvious that higher the charge migration from the surface of the ZnS semiconductor, the faster will be the degradation of the surface-attached MB. Under selective UV radiation, we have recorded the absorption peak of MB (at 655 nm) at 90 sec intervals, using SPECTRA SUITE software supplied by Ocean Optics, and plotted it against the time of photo-irradiation. The decrease in the absorbance at 655 nm implies the reduction of MB to colourless leuco methylene blue (LMB). Results of MB degradation in the presence and absence of 25 mM ZnS photocatalysts under UV light are shown in Fig. 38b, where the relative concentration (C_t/C_0) of MB in solution is plotted with respect to UV irradiation time. The percentages of total photodegradation are found to be enhanced in CHT-ZnS compared to Cys-capped NPs. This observation clearly reveals the molecular recognition of MB molecules by ZnS-attached protein, which can effectively host both ZnS and MB molecules; consequently the electron transfer process is facilitated when electron donor and acceptor molecules come to a close proximity. It is also revealed that the photocatalytic activity of photocatalyst decreases upon Mn-doping which is consistent with the fact that excited electrons

of ZnS can resonantly transfer their energy to Mn^{2+} state via nonradiative processes. As a consequence, in the presence of Mn, excited electrons are unable to migrate from the ZnS surface to perform the

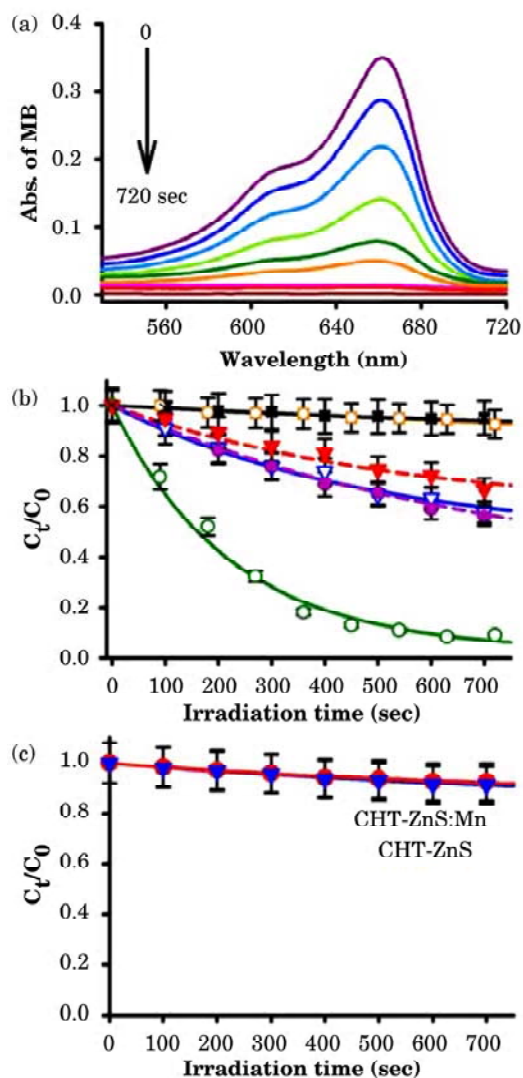


Fig. 38: (a) Time dependent UV-vis spectral changes of methylene blue (MB) in the presence of CHT-ZnS BNCs under UV-light irradiation. (b) Plot of relative concentration (C_t/C_0) versus irradiation time for the degradation of MB (monitored at 655 nm) is shown. The degradation is performed in the presence of BNCs: CHT-ZnS (empty circle), CHT-ZnS:Mn (filled circle), Cys-ZnS (empty triangle), Cys-ZnS:Mn (filled triangle), only CHT (empty square), no catalysts (crossed). (c) Plot of C_t/C_0 versus irradiation time in the presence of CHT-ZnS (filled triangle) and CHT-ZnS:Mn (filled circle) upon selective excitation with a 350 nm high-pass filter.

reduction of MB. From the photodegradation of MB in the presence of ZnS and ZnS:Mn BNCs with a 350 high pass filter, it is clearly shown that no considerable change in the absorbance peak at 655 nm takes place upon below-band-gap excitation (shown in Fig. 38c). It reveals that the electron transfer is not allowed from ZnS/ZnS:Mn to MB upon direct excitation of electrons to the trap states in BNCs.

4. CONCLUSIONS

The interface between nanomaterials and biological systems comprises a dynamic series of interactions between nanomaterial surfaces and biological entities. These interactions are shaped by a large number of forces that could determine nanomaterial's colloidal stability, physicochemical behaviour, photophysical properties etc. The most relevant parameters in the nanoparticles design are: synthesis of the inorganic core (composition, size and shape), stabilization (*i.e.* derivatization techniques towards enhanced colloidal stability in physiological media) and, lastly, functionalization with molecules of biological relevance for enhanced bioperformance. The works covered in this chapter demonstrate the impressive array of experimental techniques to synthesize various bio-nanomaterials, their further surface modification or functionalization to impart novel optical/magnetic properties. Moreover, employing a multitude of spectroscopic tools, we have investigated the characteristic nature of the interfacial interaction between nanomaterials and biological systems. Finally, we have also discussed the promising applications of these developed bio-nanomaterials in catalysis and sensing, along with the detail mechanistic insights.

5. ACKNOWLEDGEMENTS

A.G and S.S thank UGC, N.G thanks CSIR, India. We thank DST for financial grants DST/TM/SERI/2k11/103. We thank colleagues in our laboratory at S.N. Bose National Centre whose contributions over the years, acknowledged in the references, have been instrumental in the successful evolution of work in this area. In particular, we thank Dr Rupa Sarkar and Dr. S. Shankara Narayanan. We thank Mr. M.S. Bootharaju, Mr. Paulrajpillai Lourdu Xavier, Mr. Robin John and Prof. T. Pradeep (IIT Madras, India), Dr. Salim Al-Harhi, Prof. Joydeep Dutta (Sultan Qaboos University, Sultanate of Oman), Dr. N.T.K. Thanh (University College London, United Kingdom), Dr. Barnali Ghosh and Prof. A.K. Raychaudhuri (S.N. Bose National Centre) for the collaboration work.

REFERENCES

- [1] Lakowicz, J.R. (1999). *Principles of fluorescence spectroscopy*. 3rd edn, Kluwer Academic/Plenum
- [2] Goswami, N., Saha, R. and Pal, S. (2011). Protein-assisted synthesis route of metal nanoparticles: Exploration of key chemistry of the biomolecule. *J. Nanopart Res.*, 13(10): 5485–5495.
- [3] Esumi, K., Isono, R. and Yoshimura, T. (2004). Preparation of PAMAM[®] and PPI[®]metal (silver, platinum, and palladium) nanocomposites and their catalytic activities for reduction of 4-nitrophenol. *Langmuir*, 20: 237–243.
- [4] Praharaaj, S., Nath, S., Ghosh, S.K., Kundu, S. and Pal, T. (2004). Immobilization and recovery of Au nanoparticles from anion exchange resin: Resin-bound nanoparticle matrix as a catalyst for the reduction of 4-nitrophenol. *Langmuir*, 20: 9889–9892.
- [5] Saha, S., Pal, A., Kundu, S., Basu, S. and Pal, T. (2010). Photochemical green synthesis of calcium-alginate-stabilized Ag and Au nanoparticles and their catalytic application to 4-nitrophenol reduction. *Langmuir*, 26: 2885–2893
- [6] Zhang, H., Li, X. and Chen, G. (2009). Ionic liquid-facilitated synthesis and catalytic activity of highly dispersed Ag nanoclusters supported on TiO₂. *J. Mater. Chem.*, 19: 8223–8231.
- [7] El-Brolossy, T.A. *et al.* (2008). Shape and size dependence of the surface plasmon resonance of gold nanoparticles studied by Photoacoustic technique. *Euro. Phys. J.*, 153: 361–364.
- [8] Luo, J. *et al.* (2004). Spectroscopic characterizations of molecularly linked gold nanoparticle assemblies upon thermal treatment. *Langmuir*, 20: 4254–4260.
- [9] Link, S. and El-Sayed, M.A. (2000). Shape and size dependence of radiative, properties of gold nanocrystals. *Int. Rev. Phys. Chem.*, 19: 409–453.
- [10] Ung, T., Liz-Marzan, L. and Mulvaney, P. (2001). Optical properties of thin films of Au@SiO₂ particles. *J. Phys. Chem. B*, 105: 3441–3452.
- [11] Bohren, C.F. and Huffman, D.R. (1983). Absorption and scattering of light by small particles. *Absorption and Scattering of Light by Small Particles; John Wiley: New York*
- [12] Malikova, N., Pastoriza-Santos, I., Schierhorn, M., Kotov, N.A. and Liz-Marzan, L. M. (2002). Layer-by-layer assembled mixed spherical and planar gold nanoparticles: Control of interparticle interactions. *Langmuir*, 18: 3694–3697.
- [13] Drummond, P.D., Vaughan, T.G. and Drummond, A.J. (2010). Extinction times in autocatalytic systems. *J. Phys. Chem. A*, 114: 10481–10491.
- [14] Huang, Z.Y., Mills, G. and Hajek, B. (1993). Spontaneous formation of silver particles in basic 2-propanol. *J. Phys. Chem.*, 97(44): 11542–11550.
- [15] Mei, Y., Lu, Y., Polzer, F. and Ballauff, M. (2007). Catalytic activity of palladium nanoparticles encapsulated in spherical polyelectrolyte brushes and core-shell microgels. *Chem. Mater*, 19: 1062–1069.
- [16] Panigrahi, S. *et al.* (2007). Synthesis and size-selective catalysis by supported gold nanoparticles: Study on heterogeneous and homogeneous catalytic process. *J. Phys. Chem. C*, 111: 4596–4605.
- [17] Mei, Y., Sharma, G., Lu, Y. and Ballauff, M. (2005). *Langmuir*, 21: 12229–12234.
- [18] Narayanan, S.S. and Pal, S.K. (2008). Structural and functional characterization of luminescent silver[®]protein nanobioconjugates. *The Journal of Physical Chemistry C*, 112 (13): 4874–4879.

- [19] Zheng, J., Stevenson, M.S., Hikida, R.S. and Van Patten, P.G. (2002). Influence of pH on dendrimer-protected nanoparticles. *J. Phys. Chem. B*, 106(6): 1252–1255.
- [20] Henglein, A. (1993). Physicochemical properties of small metal particles in solution: “Microelectrode” reactions, chemisorption, composite metal particles, and the atom-to-metal transition. *J. Phys. Chem.*, 97(21): 5457–5471.
- [21] Haugland, R.P. and Stryer, L. (1967). (Academic press, New York, 1967).
- [22] Verma, P.K. *et al.* (2010). Superparamagnetic fluorescent nickel-enzyme nanobioconjugates: synthesis and characterization of a novel multifunctional biological probe. *J. Mater. Chem.*, 20(18): 3722–3728.
- [23] Mie, G. (1908). Beiträge zur optik trüber medien, speziell kolloidaler Metallösungen. *Ann. Phys.*, 25: 377
- [24] Zeman, E.J. and Schatz, G.C. (1987). An accurate electromagnetic theory study of surface enhancement factors for silver, gold, copper, lithium, sodium, aluminum, gallium, indium, zinc, and cadmium. *J. Phys. Chem.*, 91(3): 634–643.
- [25] Doyle, W.T. (1958). Absorption of light by colloids in alkali halide crystals. *Phys. Rev.*, 111: 1067–1072.
- [26] Wilcoxon, J.P., Martin, J.E. and Provencio, P. (2001). Optical properties of gold and silver nanoclusters investigated by liquid chromatography. *J. Chem. Phys.*, 115: 998–1007.
- [27] Kreibiga, U. and Genzelb, L. (1985). Optical absorption of small metallic particles. *Surf. Sci.*, 156: 678–700.
- [28] Hennessey, J.P. and Johnson, W.C. (1981). Information content in the circular dichroism of proteins. *Biochemistry*, 20(5): 1085–1094.
- [29] Jordan, B.J. *et al.* (2006). Stabilization of alpha-chymotrypsin at air-water interface through surface binding to gold nanoparticle scaffolds. *Soft Matter* 2: 558–560
- [30] Narayanan, S.S., Sarkar, R. and Pal, S.K. (2007). Structural and functional characterization of enzyme-quantum dot conjugates: Covalent attachment of CdS nanocrystal to alpha-chymotrypsin. *J. Phys. Chem. C*, 111: 11539–11543.
- [31] Narayanan, S.S. and Pal, S.K. (2008). Structural and functional characterization of luminescent silver-protein nanobioconjugates. *J. Phys. Chem. C*, 112: 4874–4879.
- [32] Béchet, J.J. *et al.* (1973). Inactivation of α -chymotrypsin by a bifunctional reagent, 3,4-dihydro-3,4-dibromo-6-bromomethylcoumarin. *Eur. J. Biochem.*, 35(3): 527–539.
- [33] Goswami, N. *et al.* (2011). Copper quantum clusters in protein matrix: Potential Sensor of Pb^{2+} Ion. *Anal. Chem.*, 83(24): 9676–9680.
- [34] Xie, J.P., Zheng, Y.G. and Ying, J.Y. (2009). Protein-directed synthesis of highly fluorescent gold nanoclusters. *J. Am. Chem. Soc.*, 131(3): 888–889.
- [35] Goswami, N., Makhal, A. and Pal, S.K. (2010). Toward an alternative intrinsic probe for spectroscopic characterization of a protein. *J. Phys. Chem. B*, 114(46): 15236–15243.
- [36] Si, S. and Mandal, T.K. (2007). Tryptophan-based peptides to synthesize gold and silver nanoparticles: A mechanistic and kinetic study. *Chem. Eur. J.*, 13(11): 3160–3168.
- [37] Ramasamy, P. *et al.* (2009). Size tuning of Au nanoparticles formed by electron beam irradiation of Au₂₅ quantum clusters anchored within and outside of dipeptide nanotubes. *J. Mater. Chem.*, 19: 8456–8462.

- [38] Chaudhari, K., Lourdu Xavier, P. and Pradeep, T. (2011). Understanding the evolution of luminescent gold quantum clusters in protein templates. *ACS Nano*.
- [39] Drew, S.C. and Barnham, K.J. (2011). The heterogeneous nature of Cu²⁺ Interactions with Alzheimer's Amyloid- β Peptide. *Acc. Chem. Res.*
- [40] Mathew, A., Sajanalal, P.R. and Pradeep, T. (2011). A fifteen atom silver cluster confined in bovine serum albumin. *J. Mater. Chem.*, 11205–11212.
- [41] Giri, A., Makhal, A., Ghosh, B., Raychaudhuri, A.K. and Pal, S.K. (2010). Functionalization of manganite nanoparticles and their interaction with biologically relevant small ligands: Picosecond time-resolved FRET studies. *Nanoscale*, 2(12): 2704–2709.
- [42] Broos, J. *et al.* (1995). Flexibility of enzymes suspended in organic solvents probed by time-resolved fluorescence anisotropy. Evidence that enzyme activity and enantioselectivity are directly related to enzyme flexibility. *J. Am. Chem. Soc.*, 117: 12657–12663.
- [43] Bodini, M.E., Willis, L.A., Riechel, T.L. and Sawyer, D.T. (1976). Electrochemical and spectroscopic studies of manganese(II), -(III), and -(IV) gluconate complexes. 1. Formulas and oxidation-reduction stoichiometry. *Inorg. Chem.*, 15(7): 1538–1543.
- [44] Matzapetakis, M. *et al.* (2000). Manganese citrate chemistry: Syntheses, spectroscopic studies, and structural characterizations of novel mononuclear, water-soluble manganese citrate complexes. *Inorg. Chem.*, 39(18): 4044–4051.
- [45] Aguado, F., Rodriguez, F. and Núñez, P. 2007. Pressure-induced jahn-teller suppression and simultaneous high-spin to low-spin transition in the layered perovskite CsMnF₄. *Physical Review B*, 76(9): 094417.
- [46] Williams, A.T.R., Winfield, S.A. and Miller, J.N. (1983). Relative fluorescence quantum yields using a computer-controlled luminescence spectrometer. *Analyst*, 108(1290): 1067–1071.
- [47] Lee, Y.F. and Kirchhoff, J.R. (1994). Absorption and luminescence spectroelectrochemical characterization of a highly luminescent rhenium(II) complex. *J. Am. Chem. Soc.*, 116(8): 3599–3600.
- [48] Liang, S., Teng, F., Bulgan, G. and Zhu, Y. (2007). Effect of jahn-teller distortion in La_{0.5}Sr_{0.5}MnO₃ cubes and nanoparticles on the catalytic oxidation of CO and CH₄. *J. Phys. Chem. C*, 111(45): 16742–16749.
- [49] Giri, A. *et al.* (2013). Rational surface modification of Mn₃O₄ nanoparticles to induce multiple photoluminescence and room temperature ferromagnetism. *J. Mater. Chem. C*, 1(9): 1885–1895.
- [50] Lei, S., Tang, K., Fang, Z. and Zheng, H. (2006). Ultrasonic-assisted synthesis of colloidal Mn₃O₄ nanoparticles at normal temperature and pressure. *Cryst. Growth Des.*, 6(8): 1757–1760.
- [51] Aguado, F., Rodriguez, F. and Núñez, P. (2007). Pressure-induced Jahn-Teller suppression and simultaneous high-spin to low-spin transition in the layered perovskite CsMnF₄. *Phys. Rev. B*, 76(9): 094417.
- [52] Figgis, B.N. and Hitchman, M.A. (2000). *Ligand Field Theory and Its Applications*. Wiley-VCH
- [53] Vestal, C.R. and Zhang, Z.J. (2003). Effects of surface coordination chemistry on the magnetic properties of MnFe₂O₄ spinel ferrite nanoparticles. *J. Am. Chem. Soc.*, 125(32): 9828–9833.
- [54] Li, Y. *et al.* (2011). Well shaped Mn₃O₄ nano-octahedra with anomalous magnetic behavior and enhanced photodecomposition properties. *Small*, 7(4): 475–483.

- [55] Zhang, P.Q. *et al.* (2010). Shape-controlled synthesis of Mn_3O_4 nanocrystals and their catalysis of the degradation of methylene blue. *Nano Res.*, 3(4): 235–243.
- [56] Goswami, N. *et al.* (2012). Protein-directed synthesis of NIR-emitting, tunable HgS quantum dots and their applications in metal-ion sensing. *Small*, 8(20): 3175–3184.
- [57] Xie, J.P., Zheng, Y.G. and Ying, J.Y. (2010). Highly selective and ultrasensitive detection of Hg^{2+} based on fluorescence quenching of Au nanoclusters by Hg^{2+} -Au(+) interactions. *Chem. Commun.*, 46(6): 961–963.
- [58] Guo, C.L. and Irudayaraj, J. (2011). Fluorescent Ag clusters via a protein-directed approach as a Hg(II) ion sensor. *Anal. Chem.*, 83(8): 2883–2889.
- [59] Narayanan, S.S. and Pal, S.K. (2008). Structural and functional characterization of luminescent silver-protein nanobioconjugates. *J. Phys. Chem. C*, 112(13): 4874–4879.
- [60] Goswami, N. *et al.* (2011). Copper quantum clusters in protein matrix: Potential sensor of Pb^{2+} ion. *Anal. Chem.*, 83: 9676–9680.
- [61] Singh, A.V., Bandgar, B.M., Kasture, M., Prasad, B.L.V. and Sastry, M. (2005). Synthesis of gold, silver and their alloy nanoparticles using bovine serum albumin as foaming and stabilizing agent. *J. Mater. Chem.*, 15(48): 5115–5121.
- [62] Zhou, W. and Baneyx, F. (2011). Aqueous, protein-driven synthesis of transition metal-doped ZnS immuno-quantum dots. *ACS Nano*, 5: 8013–8018.
- [63] Long, Y., Jiang, D., Zhu, X., Wang, J. and Zhou, F. (2009). Trace Hg^{2+} analysis via quenching of the fluorescence of a CdS-encapsulated DNA nanocomposite. *Anal. Chem.*, 81(7): 2652–2657.
- [64] Campos, B.B., Algarra, M., Alonso, B., Casado, C.M. and Esteves da Silva, J.C.G. (2009). Mercury(ii) sensing based on the quenching of fluorescence of CdS-dendrimer nanocomposites. *Analyst.*, 134(12): 2447–2452.
- [65] Wichiansee, W., Nordin, M.N., Green, M. and Curry, R.J. (2011). Synthesis and optical characterization of infra-red emitting mercury sulfide (HgS) quantum dots. *J. Mater. Chem.*, 21(20): 7331–7336.
- [66] Pyykko, P. (2004). Theoretical chemistry of gold. *Angew. Chem. Int. Ed.*, 43(34): 4412–4456.
- [67] Sculfort, S. and Braunstein, P. (2011). Intramolecular d10–d10 interactions in heterometallic clusters of the transition metals. *Chem. Soc. Rev.*, 40(5): 2741–2760.
- [68] Kim, M., Taylor, T.J. and Gabbai, F.P. (2008). $\text{Hg}(\text{II}) \cdots \text{Pd}(\text{II})$ Metallophilic Interactions. *J. Am. Chem. Soc.*, 130(20): 6332–6333.
- [69] Wiechelman, K.J., Braun, R.D. and Fitzpatrick, J.D. (1988). Investigation of the bicinchoninic acid protein assay – Identification of the groups responsible for color formation. *Anal. Biochem.*, 175(1): 231–237.
- [70] Sarkar, R. *et al.* (2007). Direct conjugation of semiconductor nanocrystals to a globular protein to study protein-folding intermediates. *J. Phys. Chem. B*, 111(42): 12294–12298.
- [71] He, X.M. and Carter, D.C. (1992). Atomic structure and chemistry of human serum albumin. *Nature*, 358(6383): 209–215.
- [72] Makhhal, A., Sarkar, S. and Pal, S.K. (2012). Protein-mediated synthesis of nanosized Mn-doped ZnS: A multifunctional, UV-durable bio-nanocomposite. *Inorg. Chem.*, 51(19): 10203–10210.
- [73] Fang, X. *et al.* (2011). ZnS nanostructures: From synthesis to applications. *Prog. Mater. Sci.*, 56: 175–287.

- [74] Fang, X., Wu, L. and Hu, L. (2011). ZnS nanostructure arrays: A developing material star. *Adv. Mater.*, 23: 585–598.
- [75] Zhou, W., Schwartz, D.T. and Baneyx, F. (2010). Single-pot biofabrication of zinc sulfide immuno-quantum dots. *J. Am. Chem. Soc.*, 132: 4731–4738.
- [76] Zhou, W. and Baneyx, F. (2011). Aqueous, protein-driven synthesis of transition metal-doped ZnS immuno-quantum dots. *ACS Nano*, 5: 8013–8018.
- [77] Zou, W.S., Sheng, D., Ge, X., Qiao, J.Q. and Lian, H.Z. (2011). Room-temperature phosphorescence chemosensor and rayleigh scattering chemodosimeter dual-recognition probe for 2,4,6-trinitrotoluene based on manganese-doped ZnS quantum dots. *Anal. Chem.*, 83: 30–37.
- [78] Zhuang, J. *et al.* (2003). Synthesis of water-soluble ZnS : Mn²⁺ nanocrystals by using mercaptopropionic acid as stabilizer. *J. Mater. Chem.*, 13: 1853–1857.
- [79] Deng, Z. *et al.* (2011). High-quality manganese-doped zinc sulfide quantum rods with tunable dual-color and multiphoton emissions. *J. Am. Chem. Soc.*, 133: 5389–5396.
- [80] Brus, L. E. 1983. A Simple Model for the Ionization Potential, Electron Affinity, and Aqueous Redox Potentials of Small Semiconductor Crystallites. *J. Chem. Phys.* 79: 5566
- [81] Dieckmann, Y., Clfen, H., Hofmann, H. and Fink, A.P. (2009). Particle size distribution measurements of manganese-doped ZnS nanoparticles. *Anal. Chem.*, 81: 3889–3895.
- [82] Wu, P., Miao, L., Wang, H., Shao, X. and Yan, X. (2011). A multidimensional sensing device for the discrimination of proteins based on manganese-doped ZnS quantum dots. *Angew. Chem. Int. Ed.*, 50: 8118–8121.
- [83] Bacher, G. *et al.* (2005). Spin-spin interaction in magnetic semiconductor quantum dots. *Physica E*, 26: 37–44.
- [84] Bhargava, R.N. and Gallagher, D. (1994). Optical properties of manganese-doped nanocrystals of ZnS. *Phys. Rev. Lett.*, 72: 416–419.
- [85] Sooklal, K., Cullum, B.S., Angel, S.M. and Murphy, C.J. (1994). Photophysical properties of ZnS nanoclusters with spatially localized Mn²⁺. *J. Phys. Chem.*, 100: 4551–4555.
- [86] Levy, L., Feltin, N., Ingert, D. and Pileni, M.P. (1997). Three dimensionally diluted magnetic semiconductor clusters Cd_{1-y}Mn_yS with a range of sizes and compositions: Dependence of spectroscopic properties on the synthesis mode. *J. Phys. Chem. B*, 101: 9153–9160.
- [87] Kim, M.R., Chung, J.H. and Jang, D. (2009). Spectroscopy and dynamics of Mn²⁺ in ZnS nanoparticles. *Phys. Chem. Chem. Phys.*, 11: 1003–1006.
- [88] Bol, A.A. and Meijerink, A. (1998). Long-lived Mn²⁺ emission in nanocrystalline ZnS:Mn²⁺. *Phys. Rev. B*, 58: R15997–R16000.
- [89] Smith, B.A., Zhang, J.Z., Joly, A. and Liu, J. (2000). Luminescence decay kinetics of Mn²⁺-doped ZnS nanoclusters grown in reverse micelles. *Phys. Rev. B*, 62: 2021–2028.
- [90] Tanaka, M. (2002). Photoluminescence properties of Mn²⁺-doped II–VI semiconductor nanocrystals. *J. Lumin.*, 100: 163–173.
- [91] Fujiwara, H., Hosokawa, H., Murakoshi, K., Wada, Y. and Yanagida, S. (1998). Surface characteristics of ZnS nanocrystallites relating to their photocatalysis for CO₂ reduction. *Langmuir*, 14: 5154–5159.
- [92] Xia, B., Lenggoro, I.W. and Okuyama, K. (2002). Synthesis and photoluminescence of spherical ZnS:Mn²⁺ particles. *Chem. Mater*, 14: 4969–4974.

- [93] Sarkar, S. *et al.* (2011). Photoselective excited state dynamics in ZnO–Au nanocomposites and their implications in photocatalysis and dye–sensitized solar cells. *Phys. Chem. Chem. Phys.*, 13: 12488–12496.
- [94] Baruah, S. *et al.* (2009). Photoreactivity of ZnO nanoparticles in visible light: Effect of surface states on electron transfer reaction. *J. Appl. Phys.*, 105: 074308.

